Materials Today Bio 31 (2025) 101628

Contents lists available at ScienceDirect

Materials Today Bio

journal homepage: www.journals.elsevier.com/materials-today-bio

# Microenvironment-responsive nanoparticles functionalized titanium implants mediate redox balance and immunomodulation for enhanced osseointegration

Wei Chen [a,b,c], Yifei Pan [a,b,c], Catherine Huihan Chu [d], Shuo Dong [a,b], Mingxi Wang [a], Long Wang [a], Lingxu Wang [a], Xuyang Lin [a], Chunbo Tang [a,b,c,*]

[a] Department of Oral Implantology, Affiliated Stomatological Hospital of Nanjing Medical University, Nanjing, 210029, China
[b] State Key Laboratory Cultivation Base of Research, Prevention, and Treatment for Oral Diseases, Nanjing, 210029, China
[c] Jiangsu Province Engineering Research Center of Stomatological Translational Medicine, Nanjing, 210029, China
[d] Department of Orthodontic, Affiliated Stomatological Hospital of Nanjing Medical University, Nanjing, 210029, China

ARTICLE INFO

*Keywords:*
Implants
Osseointegration
Surface modification
Reactive oxygen species regulation
Immunomodulation

ABSTRACT

Various pathological conditions (*e.g.*, diabetes, osteoporosis) are accompanied by persistent oxidative stress, which compromises the immune microenvironment and poses substantial challenges for osseointegration. Reactive oxygen species (ROS) play a "double-edged sword" role in bone tissue. Therefore, developing responsive biomaterials to maintain redox balance dynamically is crucial for enhanced osseointegration. Herein, the microenvironment-responsive coordination nanoparticles (C-Ca-SalB NPs) composed of salvianolic acid B (SalB), catechol-conjugated chitosan (CS-C), and $Ca^{2+}$ are constructed and further covalently immobilized onto titanium implant surfaces. The resulting implants achieve on-demand antioxidant and immunomodulatory effects in a microenvironment-responsive manner, thus facilitating bone regeneration under both normal and oxidative conditions. Under physiological conditions, the functionalized implants display modest immunomodulatory properties without affecting oxidative balance, while C-Ca-SalB NPs remain relatively stable. However, the modified implants enable rapid decomposition of C-Ca-SalB NPs under acidic oxidative conditions, displaying robust ROS-scavenging, anti-inflammatory, and osteoinductive capacities, ultimately remodeling the pathological microenvironment into a regenerative one. Overall, smart implants with controlled bioactive agent release in this study present a comprehensive solution for enhancing bone-implant integration, particularly in the challenging context of oxidative stress.

## 1. Introduction

Successful osseointegration is vital for the effective function of dental implants [1]. However, the intrinsic inertness of titanium and its alloys leads to inadequate osseointegration, a challenge that becomes particularly pronounced in patients with certain systemic diseases such as diabetes and osteoporosis [2,3]. The risk of implant failure in these patients is significantly increased [4], and the mechanism is closely related to the persistent oxidative stress in the microenvironment [5]. Numerous studies have confirmed that oxidative stress caused by reactive oxygen species (ROS) overproduction is one of the crucial factors affecting bone metabolism [6–8]. Notably, ROS is not always pernicious. ROS of physiological concentrations have positive biological effects; however, when the delicate balance of ROS generation and elimination is disrupted, excess ROS may trigger cell dysfunction and death [9]. Various antioxidants have been utilized to modify implants to combat oxidative stress [10,11]. Nevertheless, irrational modification schemes present the disadvantages of drug inactivation and uncontrolled drug release, the latter of which may inadvertently eliminate physiologically beneficial ROS. Consequently, developing responsive biomaterials to control redox balance smartly is scientifically important.

Recently, the complicated interactions and crosstalk between the immune and skeletal systems have attracted widespread attention. The immune system actively participates in the regulation of bone homeostasis by sharing the same microenvironment with the skeletal system [12,13]. Among various immune cells, macrophages play a significant

* Corresponding author. Department of Oral Implantology, Affiliated Stomatological Hospital of Nanjing Medical University, Nanjing, 210029, China.
*E-mail address:* cbtang@njmu.edu.cn (C. Tang).

https://doi.org/10.1016/j.mtbio.2025.101628
Received 8 December 2024; Received in revised form 27 February 2025; Accepted 1 March 2025
Available online 2 March 2025

role in immune reactions to biomaterials and serve as a critical target for modulation [14]. Besides, oxidative stress is deeply linked to inflammation [15,16]. Uncontrolled accumulation of ROS may lead to over-polarization of macrophages into the pro-inflammatory (M1) phenotype, further deteriorating the microenvironment by secreting pro-inflammatory cytokines, ROS, and acidic metabolic products, ultimately disrupting osseointegration [17]. Therefore, it is biased to focus only on the osteogenic activity of implants. Given the growing prevalence of systemic diseases, such as diabetes and osteoporosis [18], which compromise the immune system, there is an urgent need to rationally design biomaterials in light of immunomodulatory strategies to ameliorate the microenvironment and achieve favorable clinical outcomes.

Salvianolic acid B (SalB) is a polyphenolic compound with a range of biological properties, such as antioxidant, anti-inflammatory, and osteogenic effects [19]. In particular, the powerful antioxidant and anti-inflammatory capabilities of SalB make it a compelling subject of study. However, the clinical application of SalB has been primarily restricted by its poor bioavailability and easy decomposition [20]. Metal-phenolic coordination complexes are gaining popularity due to their facile fabrication, excellent biocompatibility, and pH sensitivity [21,22]. The chelation of SalB with metal ions is a valid strategy to improve the stability of SalB and realize its controllable delivery [23]. Herein, we chose $Ca^{2+}$ to be involved in the reaction for its osteoinductivity and biosafety. To further stabilize and disperse metal-phenolic assemblies, catechol-conjugated chitosan (CS-C), a derivative of chitosan (CS) with higher antioxidant activity and water solubility, was introduced into the assembly of nanoparticles [24,25].

Accordingly, in this study, we developed a microenvironment-responsive coordination nanoparticle (C-Ca-SalB NP) based on SalB, CS-C, and $Ca^{2+}$. Taking advantage of the remaining amino groups of CS-C, C-Ca-SalB NPs were further firmly immobilized on titanium surfaces (Ti-NP) through a covalent coupling tactic. We comprehensively investigated the bioactivity of our modified implants under both physiological and pathological conditions, in contrast to most studies that focus only on the performance of implants in a specific environment. Favorable results suggest that Ti-NP could regulate ROS homeostasis and the immune microenvironment in a responsive manner by on-demand drug release, thus enhancing osseointegration in both normal and acidic oxidative stress microenvironments (Scheme 1). Collectively, our novel strategy offers a comprehensive solution for enhancing osseointegration, especially under oxidative conditions, which shows broad prospects for

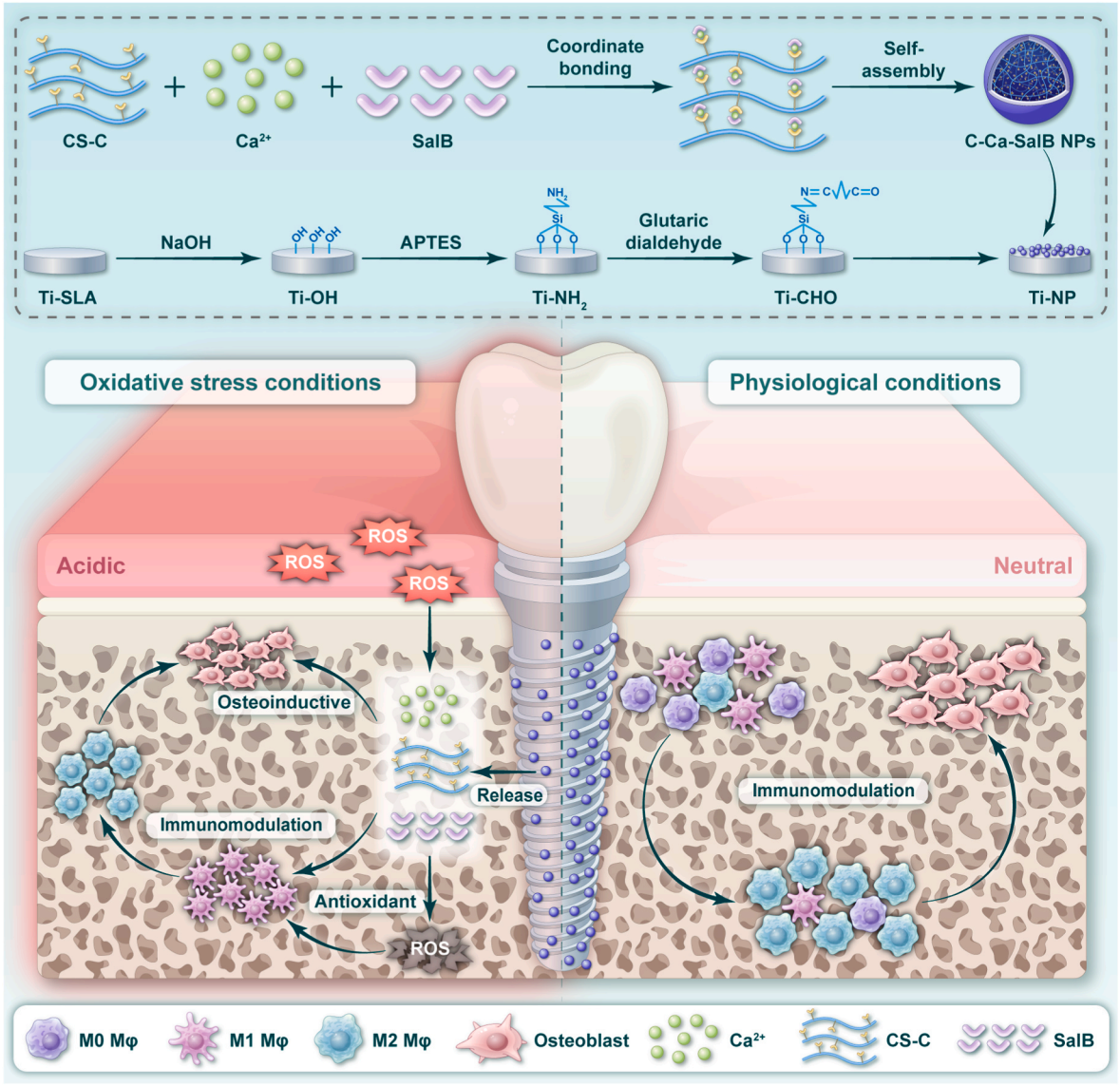


**Scheme 1.** Schematic illustration of the preparation of Ti-NP with microenvironment responsiveness and its application in promoting osseointegration under both physiological and pathological conditions.

clinical transformation.

## 2. Materials and methods

### 2.1. Materials

CS, hydrocaffeic acid (HCA), SalB, 1-ethyl-3 (3-dimethylaminopropyl) carbodiimide (EDC), (3-aminopropyl) triethoxysilane (APTES), and glutaraldehyde (GA) were purchased from Macklin (Shanghai, China). Commercially pure titanium disks and rods were purchased from Baoji Titanium (Baoji, China). Other reagents used in this study are listed in Supplementary Information (SI).

### 2.2. Sample preparation and characterization

#### 2.2.1. Preparation and characterization of CS-C

CS-C was synthesized as previously described [25,26]. Briefly, 5 mL of HCA solution (50 mg/mL) was added to the CS solution (10 mg/mL). 0.48 g EDC dissolved in 50 mL double distilled water (DDW) and ethanol mixture (1:1, v/v) was introduced into the mixture under stirring. The conjugation reaction was carried out at room temperature for 12 h (pH maintained between 4.5 and 5.0). Finally, the product was dialyzed against acidified DDW (pH 5.0) for 48 h and lyophilized. The catechol conjugation was confirmed using ultraviolet–visible (UV–Vis, Shimadzu, Japan), proton nuclear magnetic resonance ($^1$H NMR, Bruker Avance, 600 MHz, Germany), and Fourier transform infrared spectroscopy (FTIR, Nicolet IS10, Thermo Fisher, USA).

#### 2.2.2. Synthesis and characterization of C-Ca-SalB NPs

C-Ca-SalB NPs were prepared based on the host-guest theory [27]. Briefly, calcium chloride solution was added dropwise to SalB solution with the pH adjusted to 6.0. After incubating for 2 h with agitation, the mixture was transferred to CS-C solution (1.5 mg/mL), followed by adjusting the pH to 7.0. The final mixture was incubated for 6 h and then dialyzed against deionized water for 12 h. The content of SalB in the nanoparticle was determined by high-performance liquid chromatography (HPLC) assay. The result indicates that the loading efficiency was 8.66 %. Scanning electron microscopy (SEM, MAIA3, TESCAN, Czech) and transmission electron microscopy (TEM, Tecnai G2 F30, FEI, USA) were used to characterize the morphology of nanoparticles. C-Ca-SalB NPs were immersed in phosphate buffered saline (PBS) at pH 7.4 and 5.5, respectively. After 24 h, the morphology and dimensions of C-Ca-SalB NPs were observed using TEM and dynamic light scattering (DLS, Nano ZS90, Malven, UK). X-ray photoelectron spectroscopy (XPS, Escalab 250Xi, Thermo Fisher, USA) analysis was performed to detect elemental composition. The molecular dynamics (MD) simulation was conducted using GROMACS 2019.6 software. More details are provided in SI.

#### 2.2.3. Preparation and characterization of titanium samples

Titanium samples were initially polished with sandpaper. Subsequently, the polished titanium samples were sandblasted with large grit and acid-etched (SLA) according to previous studies, denoted as Ti-SLA [28]. Next, the Ti-SLA substrates were subjected to alkali-heat treatment in 5 M NaOH solution at 60 °C for 12 h to acquire the Ti-OH surfaces. After ultrasonically cleaning and drying, Ti-OH samples were modified with 2 % (v/v) APTES ethanol solution for 24 h and cured at 100 °C for 1 h, marked as Ti-$NH_2$. The resulting samples were subsequently immersed in 2 % (v/v) GA solution at 4 °C for 12 h to obtain the Ti-CHO substrates. Finally, the Ti-CHO samples were coupled with C-Ca-SalB NPs, denoted as Ti-NP. Simultaneously, a control group was prepared by treating with CS-C solution and marked as Ti-CS-C. The surface morphology and elemental mapping were characterized by SEM. Chemical states of surfaces were analyzed by XPS. The hydrophilicity of the different samples was measured using a contact angle goniometer (JC2000C1, Powereach, China). The surface roughness was detected by a 3D surface topography device (Rtec, USA). To investigate the mechanical stability of Ti-NP, cylindrical defects (1 mm in diameter, 5 mm in length) were created in rat femurs. Following repeated cycles of insertion and extraction of the titanium rods, the surface morphology was analyzed using SEM. To evaluate the responsive releasing profiles of SalB and $Ca^{2+}$ from Ti-NP, Ti-NP substrates were immersed into 5.0 mL PBS at pH 7.4 and 5.5, respectively. The specimens were collected at predetermined time intervals. The concentrations of SalB were determined by HPLC, and the content of $Ca^{2+}$ was measured using a calcium assay kit. The radical scavenging activity of different samples was investigated by 2,2-diphenyl-1-picrylhydrazyl (DPPH) and 2,2′-azino-bis (3-ethylbenzothiazoline-6-sulfonic acid) ($ABTS^+$) assays following the manufacturer's protocols.

### 2.3. In vitro biocompatibility evaluation

The cytocompatibility of different samples towards murine osteoblast-like cell line (MC3T3-E1) and murine macrophage-like cell line (RAW264.7) was characterized using cell counting kit-8 (CCK-8) and live/dead staining kits. Moreover, the hemolysis analysis of various samples was conducted according to previous studies [29]. Details are presented in SI.

### 2.4. Intracellular ROS clearance properties

RAW264.7 cells were cultured on different samples with or without 300 μM $H_2O_2$ stimulation. For intracellular ROS detection, cells were incubated with 2′,7′-dichlorodihydrofluorescein diacetate (DCFH-DA, 10 μM) at 37 °C for 30 min. Thereafter, the nuclei were stained with Hoechst and cells were observed by a fluorescence microscope. ImageJ software was applied to analyze the fluorescence intensity of DCFH-DA. The levels of superoxide dismutase (SOD) and lipid peroxidation malondialdehyde (MDA) in macrophages were detected using SOD and MDA assay kits. The expression of antioxidant-related genes (superoxide dismutase 1 (SOD1), superoxide dismutase 2 (SOD2), heme oxygenase-1 (HO-1), and nuclear factor erythroid 2-related factor 2 (Nrf2)) was examined by quantitative real-time polymerase chain reaction (qRT-PCR). mRNA expression was normalized to β-actin. The primer sequences used in the present study are listed in Table S1. More details are shown in SI.

### 2.5. In vitro immunomodulatory effect

RAW264.7 cells were cultured on different substrates with or without 300 μM $H_2O_2$ stimulation. The protein expression of inducible nitric oxide synthase (iNOS) and arginase-1 (Arg-1) was assessed by immunofluorescent staining and western blotting. The expression of M1 phenotype-related genes (iNOS, CD86, tumor necrosis factor-alpha (TNF-α), and interleukin-6 (IL-6)) and anti-inflammatory (M2) phenotype-related genes (Arg-1, CD206, interleukin-4 (IL-4), and interleukin-10 (IL-10)) were evaluated by qRT-PCR (Table S1). More details are described in SI.

### 2.6. Immunomodulation-regulated osteogenic responses in vitro

To investigate the role of Ti-NP-treated macrophages in osteogenesis, we extracted the supernatants of RAW264.7 cells incubated with different samples under normal or oxidative conditions and mixed them with osteoblast medium at a ratio of 1:1 to obtain conditioned mediums (CMs), which were used for the subsequent culture of MC3T3-E1 cells. Cell migration was measured using a transwell cell culture insert with a pore size of 8 μm. MC3T3-E1 cells were seeded onto the upper chamber without serum, and CMs were added to the lower culture plate. After culturing for 48 h, the migrated cells were fixed and stained with crystal violet solution. To assess the osteogenic differentiation of MC3T3-E1 cells cultured with CMs, alkaline phosphatase (ALP) staining, ALP

quantitative analysis, immunofluorescence staining, western blotting, and qRT-PCR were performed. For ALP staining, cells were fixed and stained with a BCIP/NBT staining kit. ALP quantitative analysis was detected with an ALP microplate test kit. The protein expression of osteopontin (OPN) was evaluated by immunofluorescence staining. Western blotting was used to detect the protein expression levels of runt-related transcription factor 2 (Runx2), osterix (OSX), and osteocalcin (OCN). The expression of osteogenic-related genes (Runx2, OSX, and OPN) was assessed by qRT-PCR. GAPDH was utilized as the housekeeping gene (Table S1).

### 2.7. In vitro osteogenic differentiation under oxidative conditions

To assess the direct effect of ingredients released from Ti-NP on osteogenic differentiation, MC3T3-E1 cells were incubated on different substrates with the stimulation of $H_2O_2$. After culturing for 7 days, ALP quantitative analysis and qRT-PCR were performed to investigate the direct osteogenic activity of different samples.

### 2.8. Animals model construction

All animal experiments were in accordance with the ARRIVE guidelines and were approved by the Animal Ethics Committee of Nanjing Medical University (IACUC-2401018). Eight-week-old male Sprague-Dawley (SD) rats were purchased from the Experimental Animal Center of Nanjing Medical University. All rats were randomly divided into two groups. One group of rats received intraperitoneal administration of 50 mg/kg streptozotocin to establish a type I diabetes mellitus (DM) model, while an equal volume of citrate buffer was injected into the other group as a healthy control group. After 7 days, rats with a blood glucose level greater than 11.1 mM were selected for the DM group. DM rats were randomly assigned to Ti-SLA, Ti-OH, and Ti-NP groups, and healthy rats were randomly assigned to Ti-SLA and Ti-NP groups. Before surgery, each rat was intraperitoneally injected with sodium pentobarbital (30 mg/kg). A cylindrical defect (1 mm in diameter, 10 mm in length) was created using a surgical drill at the distal femur of the rat, and the titanium rod was inserted in place.

### 2.9. In vivo osseointegration evaluation

Rats were sacrificed by euthanasia after 4 weeks of surgery. Collected femurs were fixed and scanned by micro-computed tomography (micro-CT) to evaluate new bone formation around the implant. The region of interest was a 2 mm long cylinder containing the implant and 200 μm of surrounding tissue, located 3.0 mm below the epiphyseal line. To perform Hematoxylin and eosin (H&E) and Masson's Trichrome staining, the fixed femurs were decalcified with 10 % ethylenediaminetetraacetic acid (EDTA) solution. Afterward, femurs were made into sections and stained using H&E and Masson's Trichrome staining kits.

### 2.10. In vivo biosafety evaluation

The hearts, lungs, liver, spleens, and kidneys from rats were collected. H&E staining was performed to assess the biosafety of different samples.

### 2.11. In vivo antioxidant and immunomodulatory evaluation

Rats were sacrificed after 1 week of implantation. Collected femurs were fixed and decalcified with 10 % EDTA solution. Immunofluorescence staining for 4-hydroxy-2-nonenal (4-HNE) and 8-hydroxydeoxyguanosine (8-OHdG) was performed to assess the antioxidant performance of different samples. Immunohistochemical staining for TNF-α and CD206 was performed to assess the immunomodulatory performance of different samples. ImageJ software was used for quantitative evaluation. Details are presented in SI.

### 2.12. Statistical analysis

All experiments were repeated at least 3 times. Statistical analyses were performed using SPSS 22.0 software. All data were expressed as mean ± standard deviation (SD). Multiple comparisons were conducted using one-way analysis of variance followed by Student-Newman-Keuls tests. Comparisons between two groups were analyzed using two-tailed independent t-tests. Statistical significance was considered at a threshold of $P < 0.05$.

## 3. Results and discussion

### 3.1. Synthesis and characterization of C-Ca-SalB NPs

We first synthesized CS-C using standard carbodiimide chemistry (Fig. S1A). The UV–Vis spectrum of CS-C showed a strong absorption peak at a wavelength of 280 nm, whereas CS showed no absorbance, indicating the conjugation of catechol groups on CS (Fig. S1B) [26]. The degree of catechol substitution was 17.53 % based on the calibration curve generated from the absorption of standard HCA solutions at 280 nm (Fig. S1C). The characteristic $^1$H NMR peak for aromatic ring protons in catechol moieties of CS-C occurred at 6.70 ppm (Fig. S1D) [30]. We further characterized the structure of CS-C by FTIR. The broad absorption peak at 3350 $cm^{-1}$ is attributed to the stretching vibration of O-H and N-H. CS presented peaks at 1650 $cm^{-1}$ and 1590 $cm^{-1}$, which belong to its amide I and II bands, respectively [31]. After the coupling reaction between CS and HCA, the strong absorption peak at 1625 $cm^{-1}$ is related to the newly formed amide bonds (C=O stretching vibration) [32]. Additionally, a characteristic peak for the stretching vibration of aromatic C=C appeared at 1518 $cm^{-1}$ (Fig. S1E) [33].These results confirmed that catechol groups had been successfully grafted onto CS. The introduction of catechol groups alters the secondary structure of the CS by breaking the intra- and inter-molecular hydrogen bonds, thus improving its water solubility, which is beneficial for the subsequent coordination reaction with metal ions. Moreover, the steric hindrance effect of CS-C is conducive to nanocomplex stabilization [34]. The successful synthesis of CS-C provides a prerequisite for the subsequent self-assembly of coordination nanoparticles.

Taking advantage of the pH sensitivity of the formation and cleavage of coordination bonds, C-Ca-SalB NPs were prepared under a pH gradient (Fig. 1A). The Ca-SalB binary complex was formed at pH 6.0; pH was then adjusted to 7.0 after adding CS-C, thus promoting chelation between CS-C and the unsaturated binding site of Ca-SalB. SEM and TEM images (Fig. 1B and C) showed that C-Ca-SalB NPs had a monodisperse spherical morphology with an average size of 58.76 nm. Elemental mapping clearly illustrates the uniform distribution of the Ca element inside the nanoparticle (Fig. 1C). On the basis of the solid spherical morphology and the homogeneous distribution of the Ca element in the nanoparticles, we speculate that C-Ca-SalB NPs might be a hybrid structure with metal-ligand coordination bonds.

XPS and FTIR were applied to further validate the coordination structure of C-Ca-SalB NPs. XPS data revealed the chemical states of different elements in the nanoparticles. As expected, the XPS wide scan spectra also confirmed the existence of the Ca element in C-Ca-SalB NPs (Fig. 1E). The high-resolution Ca 2p spectrum (Fig. 1F) displayed peaks at 347.4 eV ($2p_{3/2}$) and 350.9 eV ($2p_{1/2}$), indicating the presence of Ca-O coordination bonds [35]. Meanwhile, the O 1s spectrum possessed two peaks at 531.2 (Ca-O) and 532.8 (C-O, C=O) eV (Fig. 1G) [36]. With these results, we verified the successful formation of coordination bonds between $Ca^{2+}$ and ligands. Besides, the main peaks of C 1s and N 1s correspond to the structures of CS-C and SalB (Figs. S2A and B). We then employed FTIR to analyze the chemical constitution of C-Ca-SalB NPs. The FTIR spectrum (Fig. 1D) of SalB showed a characteristic band at 1715 $cm^{-1}$, corresponding to its carboxylic acid groups. However, this

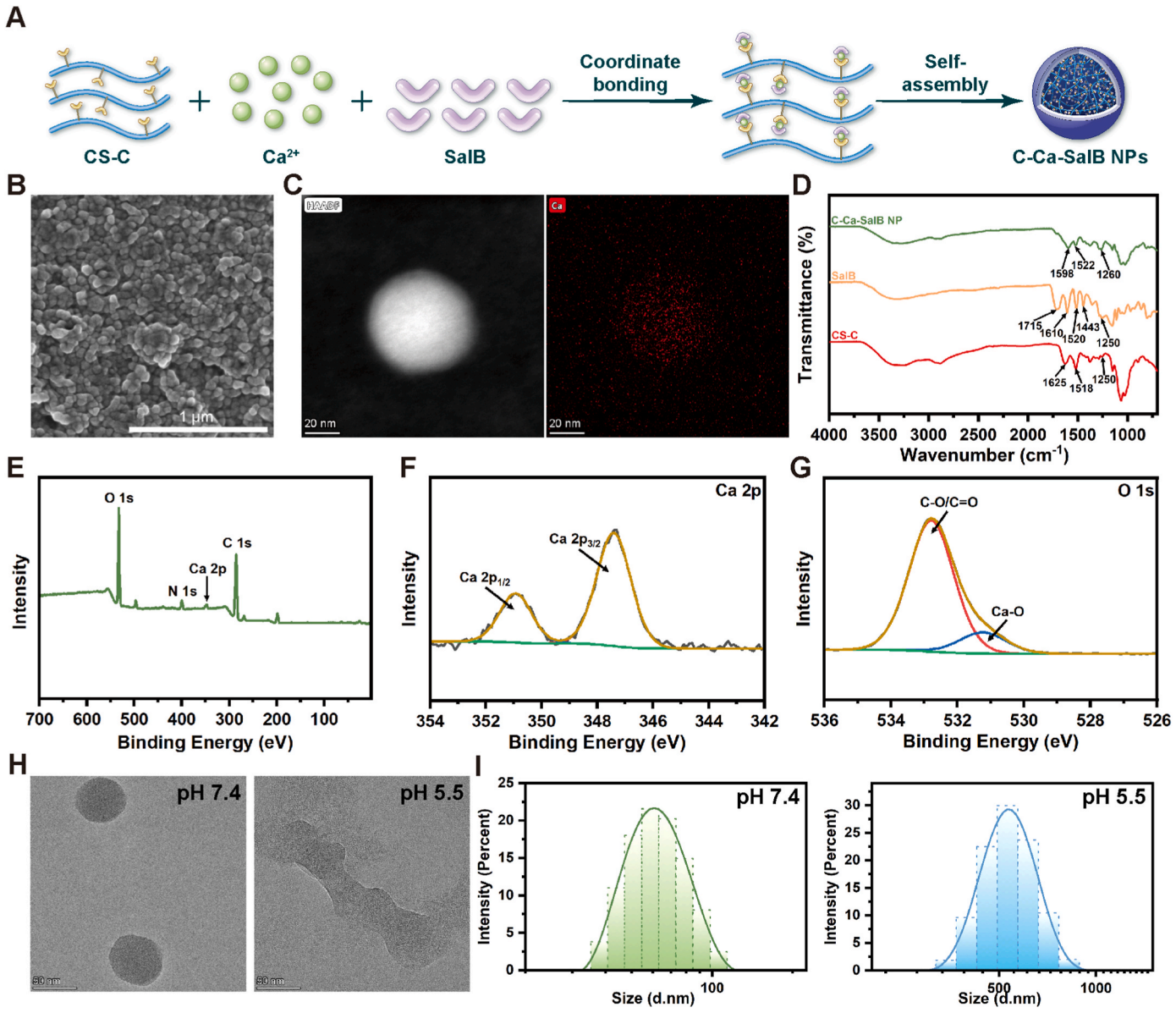


**Fig. 1.** Synthesis and characterization of C-Ca-SalB NPs. (A) Schematic scheme of C-Ca-SalB NPs. (B) A SEM image of C-Ca-SalB NPs. Scale bar: 1 μm. (C) A TEM image and elemental mapping of C-Ca-SalB NPs. Scale bar: 20 nm. (D) FTIR spectra of CS-C, SalB, and C-Ca-SalB NPs. (E) The XPS wide scan spectrum of C-Ca-SalB NPs. (F, G) High-resolution Ca 2p and O 1s XPS spectra of C-Ca-SalB NPs. (H) TEM images of C-Ca-SalB NPs under different pH conditions. Scale bar: 50 nm. (I) Hydrodynamic size distribution of C-Ca-SalB NPs under different pH conditions.

peak disappeared in the spectrum of C-Ca-SalB NPs, and a vibration representing the carboxylic acid anion appeared at 1598 $cm^{-1}$, suggesting the participation of the carboxylic acid structure of SalB during the self-assembly process. Additionally, the typical absorptions of the benzene ring in SalB, located at 1610, 1520, and 1443 $cm^{-1}$ [37], also changed in C-Ca-SalB NPs, which is linked to the variation of benzene ring substituents due to coordination bonds between $Ca^{2+}$ and phenolic hydroxyl groups. Moreover, the stretching vibration of the C-O group of catechol at 1250 $cm^{-1}$ in the spectra of CS-C and SalB shifted to 1260 $cm^{-1}$ in C-Ca-SalB NPs [38]. It can be further inferred that catechol groups in CS-C and SalB may be involved in the coordination with $Ca^{2+}$.

Subsequently, we undertook the MD simulation to illustrate the self-assembly mechanism of C-Ca-SalB NPs. Models of SalB and CS-C are displayed in Fig. S3. The root-mean-square deviation (RMSD) was calculated to reflect the system stability [39]. As shown in Fig. 2A, the system rose sharply and then stabilized after 10 ns. The solvent accessible surface area (SASA) value is regarded as a crucial index for the stability and compactness of the molecular system [40]. The initial quick aggregation of molecules led to a rapid decrease of SASA. The value tended to be stable after 30 ns, disclosing that a condensed and stable aggregation had formed (Fig. 2B). The self-assembly process of the composite system into a stable spheroidal nanocluster structure is displayed in Fig. 2D. To better understand the driving force in the self-assembly process, we next analyzed the number of hydrogen bonds, binding energy, and intermolecular interactions. Hydrogen bonds were mainly formed between CS-C molecules and between CS-C and SalB molecules (Fig. 2C). Additionally, the binding energy analysis indicated that electrostatic force was the main driving force of the self-assembly process between CS-C and SalB, followed by van der Waals force (Fig. S4). In addition to hydrogen bonds, coordination bonds might play an essential role in the self-assembly process as well. According to the analysis of intermolecular binding modes (Fig. 2E), $Ca^{2+}$ could form coordination bonds with SalB; CS-C and SalB can also be bonded through coordination bonds formed with $Ca^{2+}$. The MD simulation clearly

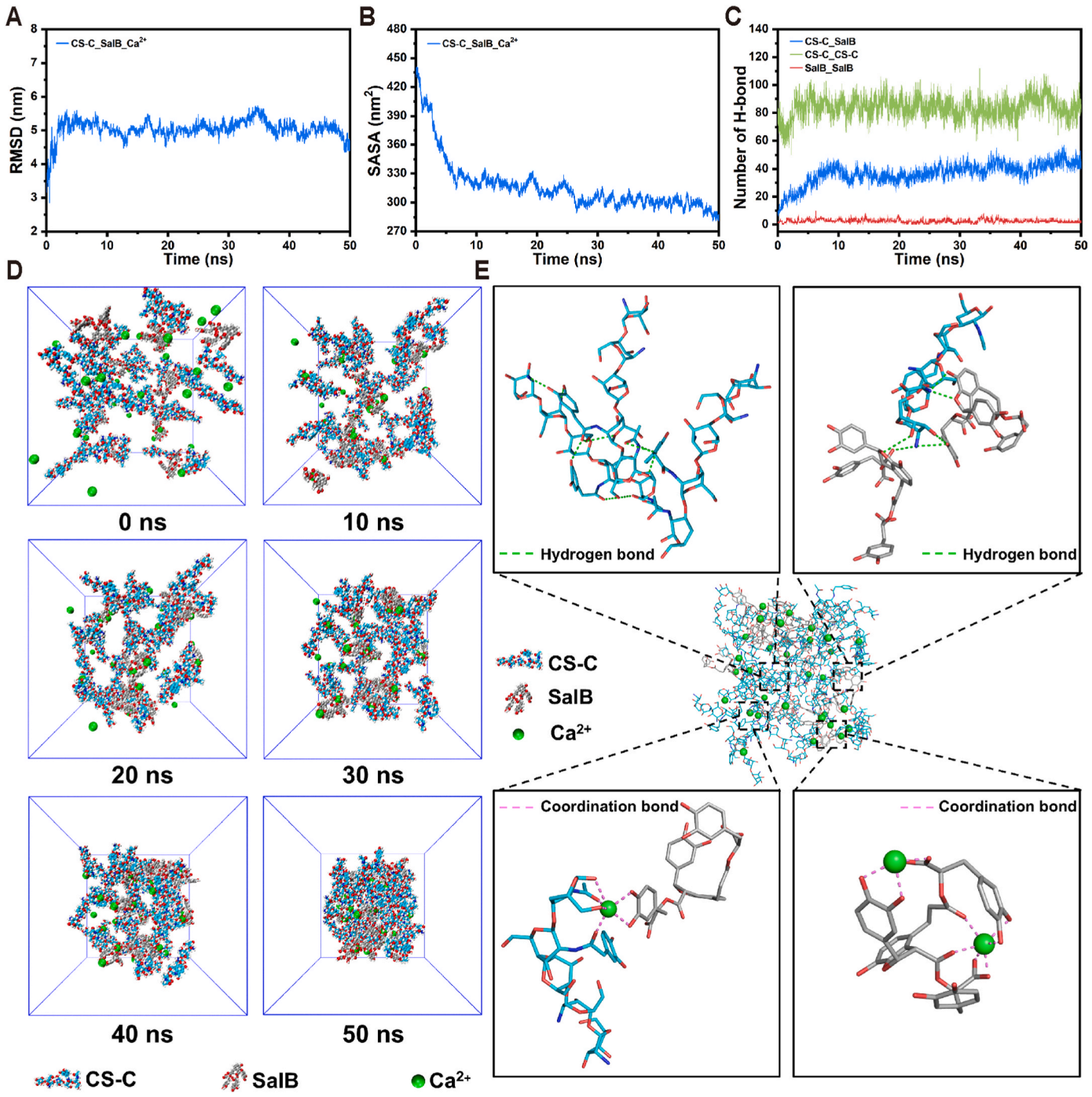


**Fig. 2.** The self-assembled mechanism of C-Ca-SalB NPs by MD simulation. (A) Time-dependent changes of RMSD in the self-assembly process. (B) Time-dependent changes of SASA in the self-assembly process. (C) The number of hydrogen bonds between CS-C, SalB, and $Ca^{2+}$. (D) The self-assembly process of C-Ca-SalB NPs. (E) The intermolecular interaction of CS-C, SalB, and $Ca^{2+}$ under a stable state (50 ns).

elucidates the self-assembly process and mechanism of C-Ca-SalB NPs, which is aligned with the above experimental results, indicating that C-Ca-SalB NPs may be a hybrid structure mainly tailored by coordination and hydrogen bonds.

Various factors, including diabetes, osteoporosis, and inflammation, may contribute to oxidative stress in the tissues surrounding implants [41]. The prolonged elevation of ROS levels leads to cell dysfunction and triggers the overproduction of acidic metabolic products, leading to a decrease in local pH, which can serve as the basis for responsive biomaterials to regulate microenvironmental homeostasis [9,42,43]. Given that C-Ca-SalB NPs is a coordination complex, we investigated its pH responsiveness by detecting changes in morphology and hydrodynamic size under different pH conditions (Fig. 1H and I). Under normal conditions (pH 7.4), C-Ca-SalB NPs exhibited a uniform spheroid shape with a hydrodynamic size of 63.5 nm. However, after being subjected to acidic conditions (pH 5.5) for 24 h, C-Ca-SalB NPs displayed an irregular morphology with signs of aggregation, and the hydrodynamic size increased to 543.0 nm. It may be ascribed to the fact that CS-C and SalB are protonated under the acidic microenvironment, leading to the cleavage of coordination bonds and the disassembly of nanoparticles. The pH responsiveness of C-Ca-SalB NPs provides potential advantages for its application in drug delivery systems.

### 3.2. Preparation and characterization of C-Ca-SalB NPs modified titanium surfaces

SLA is currently the most popular surface treatment for commercial dental implants [44]. SLA creates a micron-sized titanium surface that mimics the hierarchical scales observed at natural bone remodeling sites, resulting in enhanced osseointegration [45]. Silane coupling is a facile and universal strategy to immobilize biomolecules onto titanium surfaces [46,47]. It is generally believed that chemical immobilization through covalent bonds has better stability and strength than physical adsorption [48–50]. Accordingly, in the present study, we integrated C-Ca-SalB NPs onto the hierarchical microstructure of SLA titanium via a covalent coupling tactic. The preparation process of the functionalized surfaces from Ti-SLA is illustrated in Fig. 3A. Multiple types of characterization substantiated the successful conjugation of the nanoparticles on titanium surfaces.

As shown in Fig. 3B, SEM images showed the uniform micro-scale pits of Ti-SLA. After alkali-heat treatment, the titanium substrate presented a micro-nano composite structure. The graft of amine groups, aldehyde groups, or CS-C did not significantly change the porous microstructure. In contrast, uniform spherical nanoparticles with an average size of 57.64 nm were detected on Ti-NP surfaces, indicating the effective immobilization of C-Ca-SalB NPs. Roughness did not differ significantly between these groups, demonstrating that the functionalization of Ti-SLA merely altered the surface morphology at the nanoscale rather than the microscale (Fig. S5A). Moreover, after alkali heat treatment, the hydrophobic Ti-SLA formed a superhydrophilic surface with a contact angle of 6.55° on account of the increase of hydrophilic OH groups on titanium surfaces. Further grafting on Ti-OH maintained good surface wettability despite a slight increase in the contact angle (Fig. S5B). The changes of surface wettability are in good accordance with the variation of chemical structures.

We then conducted XPS analyses to explore the surface chemistry during the modification procedure. XPS wide scan spectra showed the changes in elemental compositions (Fig. 3C). Alkali-heat treatment of Ti-SLA led to a remarkable increase of the O 1s peak. After APTES modification, Si 2p, Si 2 s, and N 1 s signals appeared. The successful grafting of C-Ca-SalB NPs resulted in the appearance of the Ca element and a distinct increase of the C 1s peak. The conclusion was also validated by elemental mapping (Fig. S5C). High-resolution XPS spectra ulteriorly revealed the evolution of chemical bonds and chemical valence states. It has been well established that titanium implants are subjected to hydrocarbon contamination when exposed to air, which could explain the detection of carbon and nitrogen on Ti-SLA and Ti-OH surfaces [51,52]. The O 1 s signal of the Ti-SLA was deconvoluted into three peaks at 530.1, 531.2, and 532.1 eV, which are assigned to $TiO_2$, hydroxy (-OH) groups, and carbon contamination, respectively. After alkali-heat treatment, the titanium surface generated vast -OH groups. Silanization resulted in new peaks of $NH_3^+$ (399.2 eV) and -$NH_2$ (401.1 eV) in the N 1s spectrum, and Si-O (532.2 eV) in the O 1s spectrum, suggesting the interaction between the ethoxy groups in APTES and -OH groups on Ti-OH. The Schiff base reaction between APTES and GA generated a C=N-C (398.8 eV) peak in the N 1s spectrum [53]. A series of pretreatments of Ti-SLA contributes to the formation of aldehyde groups on the titanium surface, which provide anchors for the remaining amino groups of C-Ca-SalB NPs. After immobilization with CS-C and C-Ca-SalB NPs, the changes in Ca 2p, O 1s, and C 1s spectra corresponded to the structure of the substances immobilized on titanium surfaces (Fig. 3D and E).

Additionally, we assessed the mechanical stability of Ti-NP by simulating potential mechanical stresses during implant surgery (Fig. S6A). Following mechanical insertion and extraction, the surface exhibited minimal changes, maintaining a uniform distribution of nanoparticles, which demonstrated the exceptional mechanical stability of Ti-NP (Fig. S6B). This stability can be ascribed to the covalent grafting of C-Ca-SalB NPs [48,49]. Overall, the Ti-NP surfaces exhibit resistance to friction, satisfying the requirements for application in implantable medical devices.

Considering the pH responsiveness of C-Ca-SalB NPs, we further monitored the release behavior of Ti-NP at different pH values (5.5 and 7.4). Ti-NP demonstrated considerable stability at pH 7.4, with a SalB cumulative release below 20 % within 7 days. In contrast, accelerated SalB release occurred under acidic conditions (pH 5.5), with a cumulative release approximately four times higher than that observed under neutral conditions (Fig. 3F and G). As expected, similar $Ca^{2+}$ release kinetics were also detected. This phenomenon can be attributed to the disassembly of C-Ca-SalB NPs on the Ti-NP surfaces under acidic conditions. Notably, the release rate and amount of both SalB and $Ca^{2+}$ increased significantly during the first 3 days and plateaued after 5 days. However, SalB release did not exceed 65 % under any conditions within 7 days, which might be due to the reversible coordination bonds as well as the effect of hydrogen bonds. This acid-triggerable release mode has multiple benefits. On the one hand, it can maintain the activity of biomolecules during the process of implant manufacturing and storage. On the other hand, compared with traditional surface functionalization methods, our strategy facilitates on-demand release of therapeutic ingredients, thereby reducing side effects and enabling precision treatment. In an acidic pathologic microenvironment, the rapid release of SalB contributes to its antioxidant and immunomodulatory properties, while the release of $Ca^{2+}$ might promote subsequent osteogenic effects.

SalB possesses nine phenolic hydroxyls, exerting a strong free radical scavenging ability. Hence, we evaluated the maximized radical scavenging properties of Ti-NP by DPPH and $ABTS^+$ scavenging assays. As presented in Fig. 3H, Ti-NP exhibited a strong scavenging efficiency (65.97 %) against DPPH free radicals, with the color of the DPPH solution shifted from purple to deep yellow. A semblable profound effect was observed in the elimination of $ABTS^+$ radicals by Ti-NP, reflected in the change of the original blue-green color of the $ABTS^+$ solution to colorless (Fig. 3I). Notably, despite the radical eliminating ability of Ti-CS-C being significantly lower than that of Ti-NP, it still displayed 30.24 % DPPH and 48.05 % $ABTS^+$ clearance rates. This may be related to the grafting of the antioxidant catechol groups onto CS-C. Therefore, the prominent ROS scavenging ability of Ti-NP originates from the synergistic effect of SalB and CS-C. To reveal the long-term radical eliminating ability of titanium substrates, the samples were stored for 6 weeks before conducting DPPH and $ABTS^+$ assays. Ti-NP samples retained their radical scavenging effect even after 6 weeks of storage, which is of great significance for clinical applications (Fig. 3H and I). Overall, Ti-NP substrates demonstrate great potential in combating oxidative stress.

### 3.3. In vitro biocompatibility evaluation

Biocompatibility is a basic requirement for biomedical applications of implants. We evaluated the cytotoxicity of different samples towards MC3T3-E1 and RAW264.7 cells by live/dead staining and CCK-8 assays. Since the little effect of the silane coupling strategy on the biological performance of titanium surfaces has been well established, we excluded Ti-$NH_2$ and Ti-CHO groups in subsequent cell experiments [48,53,54]. Live/dead staining results illustrated that dead cells with red fluorescence were rarely observed on all substrates (Figs. S7A and B), demonstrating excellent cytocompatibility. As shown in Figs. S7C and D, MC3T3-E1 and RAW264.7 cells exhibited similar cell proliferation on all samples, respectively. We further assessed the hemocompatibility of different samples using the hemolysis assay. All experimental groups hardly displayed lysis with less than 5 % hemolysis rates, indicating excellent hemocompatibility (Fig. S7E). In conclusion, our functionalized titanium implants display favorable biocompatibility and are suitable for future clinical practice.

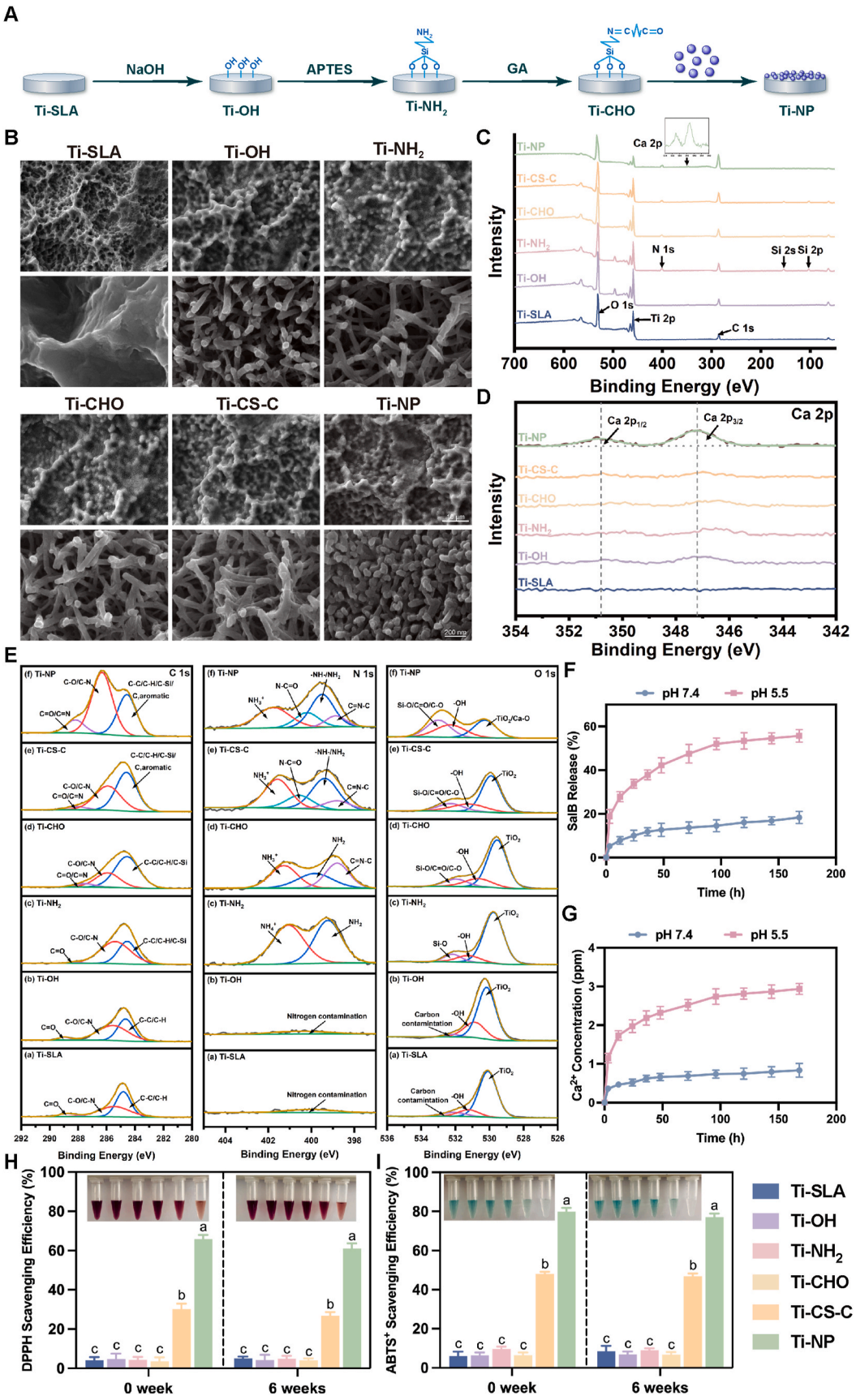


**Fig. 3.** Synthesis and characterization of variant titanium samples. (A) Synthesis procedure of Ti-NP. (B) SEM images of different functionalized titanium substrates. Scale bars: 10 μm and 200 nm. (C) XPS wide scan spectra of different samples. (D, E) Ca 2p, C 1s, N 1s, and O 1s high-resolution XPS spectra of different samples. (F, G) Cumulative release profiles of SalB and $Ca^{2+}$ from Ti-NP at different pH values. (H, I) The short-term and long-term DPPH and $ABTS^{+}$ scavenging abilities of different samples. Bars with different superscript letters indicate statistical differences ($P < 0.05$).

### 3.4. Intracellular ROS clearance properties of Ti-NP under different conditions

Immune cells represented by macrophages exert significant effects on bone regeneration and remodeling [55]. Encouraged by the promising free radical scavenging ability of Ti-NP, we further investigated the intracellular ROS clearance capability of Ti-NP under both normal and oxidative stress conditions.

We first evaluated the antioxidant performance of Ti-NP under normal conditions. Intracellular ROS levels in RAW264.7 cells were detected using the ROS indicator DCFH-DA. Modest ROS-characteristic signals were observed on all surfaces, with quantitative analysis showing enhanced fluorescence intensity in the Ti-SLA and Ti-OH groups (Fig. 4A and B). Additionally, we assessed the expression of antioxidant-related factors and genes to explore changes in the endogenous antioxidant system of macrophages. SOD is one of the critical intracellular antioxidant enzymes [9]. SOD activity in the Ti-SLA and Ti-OH groups was lower than that in the Ti-CS-C and Ti-NP groups, while MDA content, a lipid peroxidation product, showed an opposite trend (Fig. 4C and D). No statistical difference was observed in ROS, SOD, and MDA levels between the TCPS, Ti-CS-C, and Ti-NP groups, suggesting that the Ti-CS-C and Ti-NP surfaces would not impair redox homeostasis in macrophages (Fig. 4B–D). However, the Ti-SLA and Ti-OH surfaces induced an increase in intracellular ROS, consistent with previous studies [5,56]. This may be attributed to the immune response of macrophages to the physicochemical properties of the biomaterials. The rough surfaces of Ti-SLA and Ti-OH could induce ROS generation in macrophages, whereas the presence of amide and catechol groups on Ti-CS-C and Ti-NP surfaces counteract this disadvantage. The mRNA levels of antioxidant-related genes (SOD1, SOD2, HO-1, and Nrf2) also confirmed the moderate antioxidant activity of Ti-CS-C and Ti-NP under normal conditions (Fig. 4E).

To establish cellular models of oxidative stress, $H_2O_2$ was added to the culture medium to stimulate cells. $H_2O_2$ is one of the most common ROS. $H_2O_2$-induced oxidative stress has been widely regarded as a classical model that encompasses most instances of oxidative stress [5]. Consistent with previous studies, we found that 300 μM $H_2O_2$ could trigger an overproduction of ROS and initiate oxidative stress in macrophages (Fig. 4A) [5,57]. After $H_2O_2$ exposure, abundant intracellular green fluorescence signals were detected in Ti-SLA, Ti-OH, and Ti-CS-C groups, demonstrating a large amount of ROS accumulation in macrophages. Conversely, Ti-NP strongly reduced the positive expression, indicating its effective ROS-scavenging properties (Fig. 4A and B). Additionally, Ti-NP can protect the endogenous antioxidative system of macrophages from harmful ROS. As expected, Ti-NP effectively elevated SOD activity while suppressing MDA levels in co-incubated macrophages (Fig. 4C and D). Moreover, the expression of the antioxidase and related regulator genes (SOD1, SOD2, HO-1, and Nrf2) was significantly increased in the Ti-NP group (Fig. 4E). Interestingly, albeit the Ti-CS-C substrate displays a moderate radical scavenging effect, its limited antioxidative activity is insufficient to resist intense oxidative damage. Furthermore, no substantial antioxidant activity of $Ca^{2+}$ has been demonstrated in previous studies [35]. Therefore, we assume that the excellent antioxidant effect of Ti-NP in the oxidative stress environment may mainly originate from the accelerated delivery of SalB at acidic pH. SalB, with its intrinsic antioxidative properties, can directly scavenge excessive ROS. Besides, SalB can maintain intracellular oxidative balance by repairing the endogenous antioxidative function of macrophages. The synergistic action of both exogenous and endogenous antioxidation contributes to the substantial antioxidant capability of Ti-NP under oxidative stress, thus protecting cells from ROS damage.

### 3.5. In vitro immunomodulatory effect of Ti-NP under different conditions

Macrophages with plasticity can rapidly shift their phenotypes in response to biomaterials and the surrounding environment, thereby secreting corresponding cytokines to regulate the local immune microenvironment [17,58]. Notably, ROS overproduction hinders the transformation of macrophages from M1 to M2, resulting in persistent inflammation and impaired osseointegration [59]. Consequently, the timely polarization of macrophages to the M2 phenotype is essential for creating a favorable immune microenvironment for osseointegration.

We explored the immunomodulatory potential of Ti-NP *in vitro* under both normal and oxidative conditions. First, the macrophage status was characterized by detecting iNOS (M1 marker) and Arg-1 (M2 marker). Without $H_2O_2$ treatment, macrophages in Ti-CS-C and Ti-NP groups showed lower expression of iNOS positive protein and higher expression of Arg-1 positive protein, which was confirmed by immunofluorescent staining and western blotting (Fig. 5A and B). Moreover, with qRT-PCR evaluation, we evaluated the expression of inflammation-related markers from a genotypic perspective. Fig. 5C shows that the Ti-CS-C and Ti-NP groups displayed a similar trend of anti-inflammation polarization. However, under oxidative stress, macrophages showed obvious iNOS positive fluorescence and weak Arg-1 positive fluorescence in Ti-SLA, Ti-OH, and Ti-CS-C groups due to the $H_2O_2$-stimulated inflammatory response (Fig. 5D). Meanwhile, fluorescence intensity quantitative results showed that there was no statistical difference in the expression levels of iNOS or Arg-1 among the above-mentioned three groups. In contrast, Ti-NP notably reduced iNOS and increased Arg-1 levels in macrophages (Fig. 5G and H). The protein expression changes of iNOS and Arg-1 stimulated by Ti-NP were also confirmed by western blotting analyses (Fig. 5E). The same polarization trend can be found in qRT-PCR analyses of inflammation-related genes (Fig. 5F). Under $H_2O_2$ stimulus, macrophages incubated with Ti-NP exhibited significant downregulation of M1 phenotype-related genes (iNOS, CD86, TNF-α, and IL-6), along with remarkable upregulation of M2 phenotype-related markers (Arg-1, CD206, IL-4, and IL-10).

Combining the results of antioxidant and immunomodulatory effects, we believe that under normal conditions, Ti-CS-C and Ti-NP exert moderate immunomodulatory effects without affecting ROS homeostasis due to the presence of appropriate antioxidant catechol groups on their surfaces. However, with oxidative stimulation, Ti-NP reprograms the macrophage phenotype from M1 to M2 by scavenging exogenous ROS and recovering the endogenous antioxidative system. In summary, the Ti-NP surface exhibits favorable immunomodulatory properties under both normal and oxidative conditions, thereby establishing a solid foundation for the regenerative phases of bone healing.

### 3.6. Immunomodulation-regulated osteogenic responses in vitro

Successful bone healing is inseparable from the synergistic crosstalk between the immune and skeletal systems [60]. Macrophages secrete various inflammatory factors and chemokines into the surrounding microenvironment, thereby managing behaviors of downstream regenerative effector cells, which further dictates the fate of implants [61,62]. The exceptional immunomodulatory properties of Ti-NP let us further explore the role of Ti-NP-treated macrophages in osteogenesis. To this end, we extracted the supernatants of macrophages cultured with different substrates under normal or oxidative conditions for culturing MC3T3-E1 osteoblast precursor cells (Fig. S8A).

First, the osteogenic responses of MC3T3-E1 cells in CM under normal conditions were investigated. The migration capability of osteoblasts in CMs was detected by the Transwell invasion assay. As shown in Fig. 6A, a markedly larger number of MC3T3-E1 cells were recruited in the Ti-CS-C and Ti-NP groups compared to the other two groups, which shared a parallel tendency with the immunomodulatory effect. ALP staining and quantitative analysis illustrated that the Ti-CS-C and Ti-NP groups displayed stronger osteogenic potential (Fig. 6B and Fig. S8B). Besides, we assessed the effect of CMs on osteogenic differentiation at both genetic and protein levels. The upregulation of osteogenic-related genes (Runx2, OPN, and OSX) was highest in the Ti-CS-C and Ti-NP groups (Fig. 6D). Western blotting and

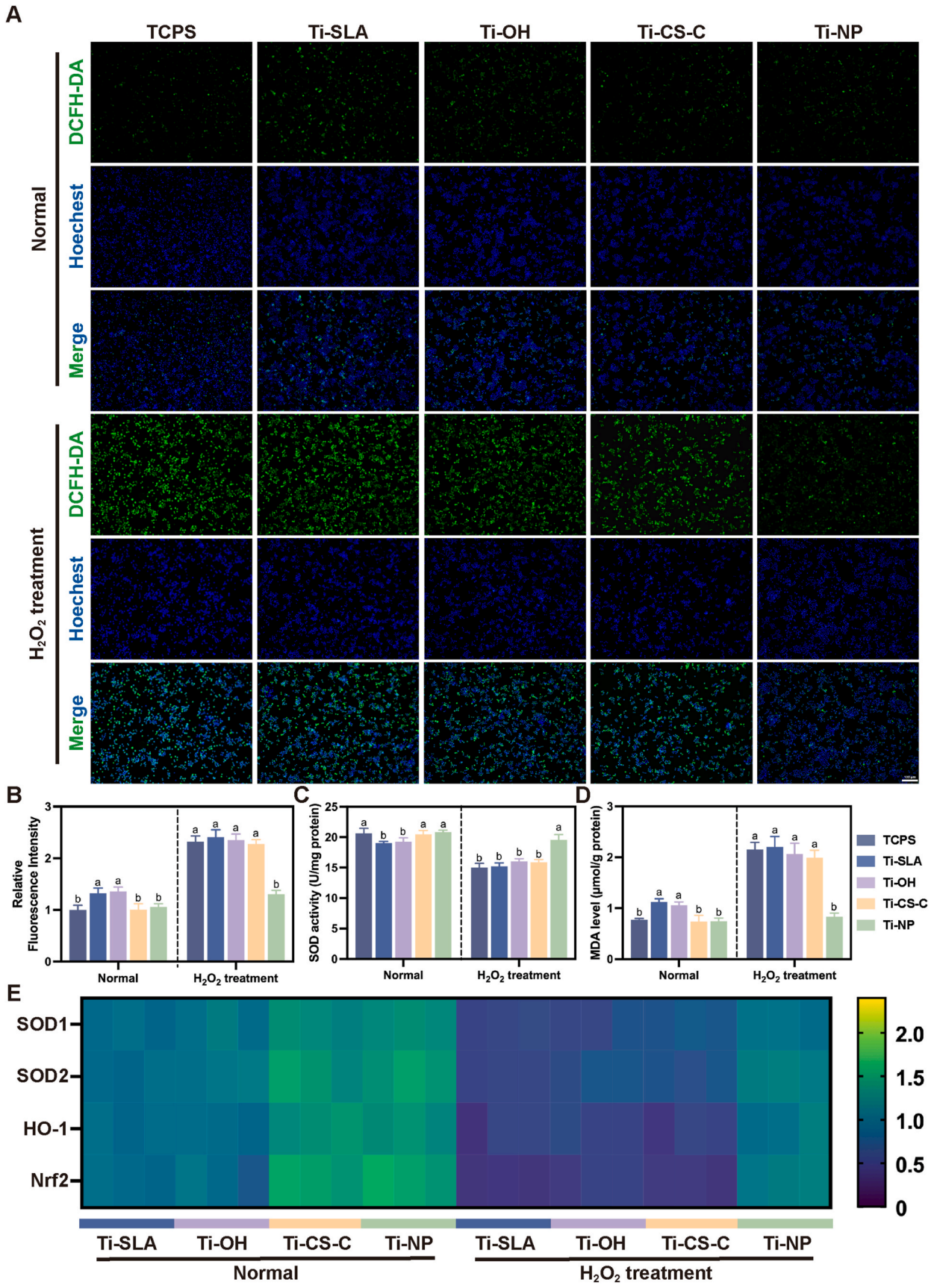


**Fig. 4.** Intracellular ROS scavenging properties of different titanium samples under normal and oxidative conditions. (A) DCFH-DA staining of macrophages with different treatments. Scale bar: 100 μm. (B) Relative fluorescence intensity corresponding to intracellular ROS levels. (C) SOD activity of macrophages with different treatments. (D) MDA levels of macrophages with different treatments. (E) Heat map for expression analysis of antioxidant-related genes (SOD1, SOD2, HO-1, and Nrf2). Bars with different superscript letters indicate statistical differences ($P < 0.05$).

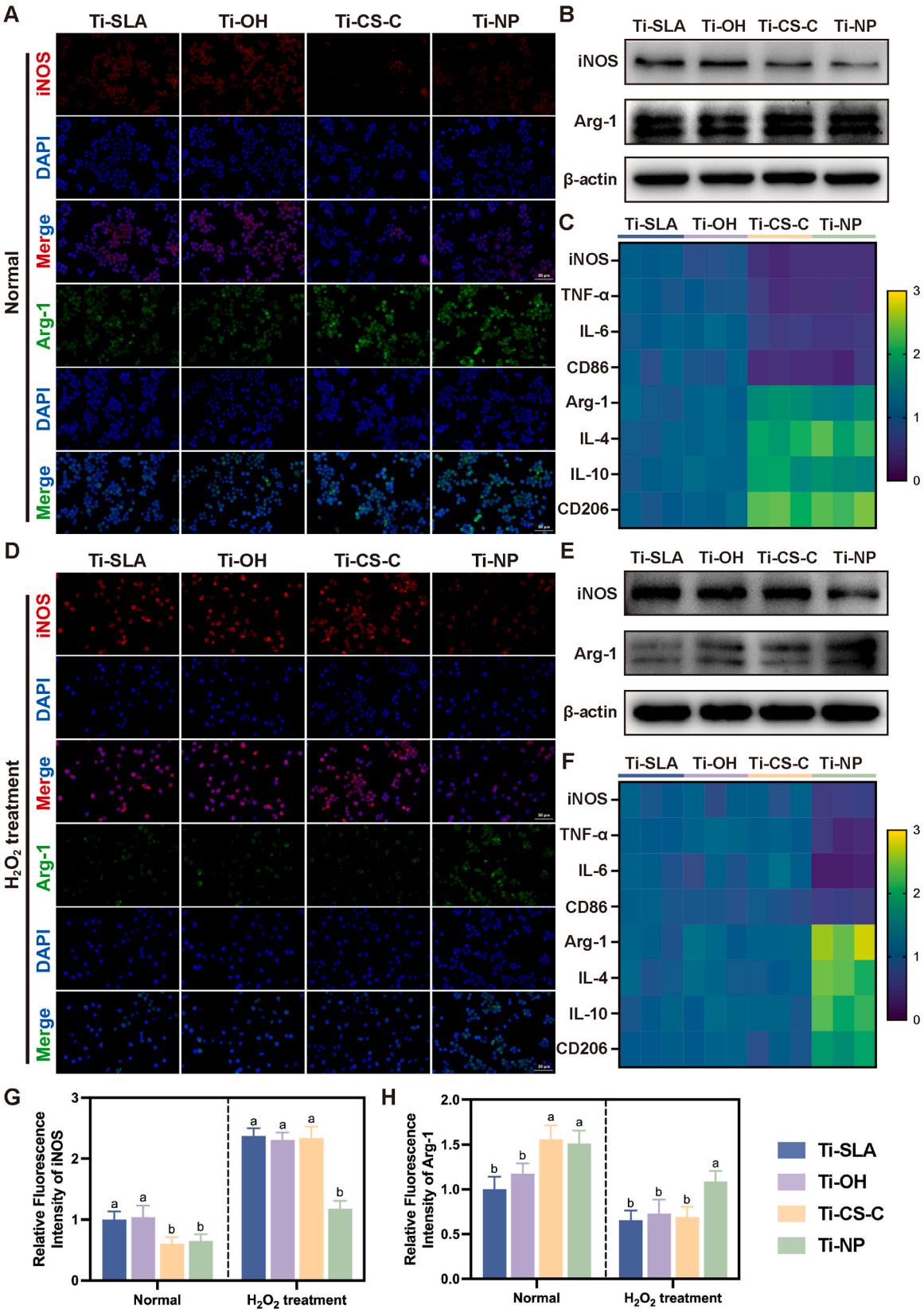


**Fig. 5.** *In vitro* immunomodulatory effect of different titanium samples under normal and oxidative conditions. (A, D) Immunofluorescent staining of iNOS and Arg-1 in macrophages cultured under different conditions. Scale bar: 50 μm. (B, E) The protein expressions of iNOS and Arg-1 in macrophages cultured under different conditions. (C, F) Heat maps for expression analysis of M1 phenotype-related genes (iNOS, CD86, TNF-α, and IL-6) and M2 phenotype-related markers (Arg-1, CD206, IL-4, and IL-10) under different conditions. (G, H) Relative fluorescence intensity corresponding to iNOS and Arg-1 levels under different conditions. Bars with different superscript letters indicate statistical differences ($P < 0.05$).

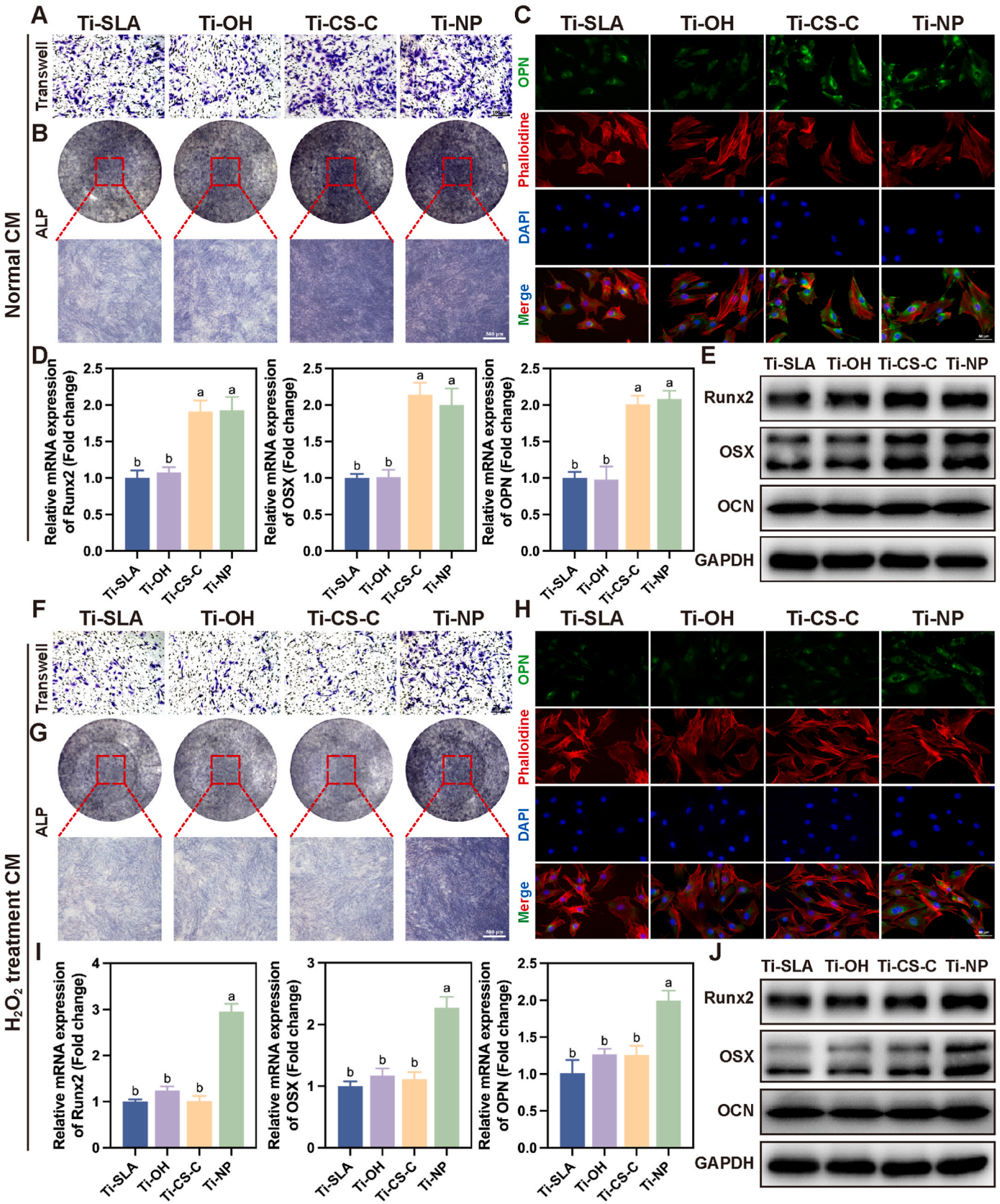


**Fig. 6.** *In vitro* effects of normal and $H_2O_2$-treated CMs on osteogenic responses of MC3T3-E1 osteoblasts. (A, F) Crystal violet staining of migrated osteoblasts cultured with normal and $H_2O_2$-treated CMs. Scale bar: 100 μm. (B, G) ALP staining of osteoblasts cultured with normal and $H_2O_2$-treated CMs. Scale bar: 500 μm. (C, H) Immunofluorescent staining of OPN in osteoblasts cultured with normal and $H_2O_2$-treated CMs. Scale bar: 50 μm. (D, I) Expressions of osteogenesis-related genes (Runx2, OSX, and OPN) of osteoblasts cultured with normal and $H_2O_2$-treated CMs. (E, J) The protein expressions of Runx2, OSX, and OCN in osteoblasts cultured with normal and $H_2O_2$-treated CMs by western blotting. Bars with different superscript letters indicate statistical differences ($P < 0.05$).

immunofluorescence staining further examined the expression of osteogenic-related proteins. As expected, enhanced expression of osteogenic-related proteins (OPN, Runx2, OSX, and OCN) was detected in the Ti-CS-C and Ti-NP groups (Fig. 6C and E, and S8C). In conclusion, CMs derived from T i-CS-C and Ti-NP exhibit superior osteoinductive effects, which might mainly be attributed to the favorable immune microenvironment generated by macrophage polarization.

Subsequently, we explored the role of $H_2O_2$-treated CMs in osteoblast behavior. Fig. 6F shows that CM collected from the Ti-NP group recruited the most MC3T3-E1 cells. The largest ALP-positive regions were found in the Ti-NP group (Fig. 6G), as confirmed by the quantitative analysis of ALP activity (Fig. S6B). Additionally, the mRNA expression of osteogenic markers (Runx2, OSX, and OPN) was upregulated in the Ti-NP group but not in the other groups, the difference being significant (Fig. 6I). Meanwhile, the OPN immunofluorescence staining further verified that Ti-NP-derived CM strongly enhanced the osteogenic activity of osteoblasts (Fig. 6H). An analogical trend was also found in the expression levels of Runx2, OSX, and OCN by western blotting (Fig. 6J and S8D). The above data suggest that CM derived from Ti-NP exerted a positive effect on osteogenesis under oxidative stress. Its potential mechanism can be summarized into two aspects. On the one hand, Ti-NP can effectively orchestrate a transition of macrophages toward the M2 phenotype through the responsive elimination of ROS, thereby reshaping the oxidative microenvironment into a more regenerative one and indirectly regulating osteogenic behaviors. On the other hand, SalB and $Ca^{2+}$, which are rapidly released in acidic conditions, have a direct promoting effect on osteogenesis (Fig. S9) [63–65]. Collectively, the macrophage CM collected from Ti-NP under oxidative stress, which includes cytokines (IL-4, IL-10, etc.) and extracts from the implant (SalB/$Ca^{2+}$), has an outstanding effect in promoting osseointegration.

### 3.7. In vivo osseointegration and biosafety evaluation

Inspired by the efficacy of Ti-NP in osteogenesis under both physiological and pathological conditions *in vitro*, we examined its osteogenic activity *in vivo* using the femoral defect implantation model. Previous studies have documented that implant surgery would inevitably induce temporary oxidative stress, making it difficult to simulate an entirely normal environment *in vivo* [66,67]. Therefore, we mainly focused on the osteogenic performance of Ti-NP in a type 1 DM rat model, which is one of the classical *in vivo* models of oxidative stress [5]. Procedures for *in vivo* evaluation are displayed in Fig. 7A. After implantation for 4 weeks, *in vivo* osseointegration was analyzed by micro-CT and histological staining. Micro-CT images revealed that more trabecular microarchitecture of bone tissue was formed around Ti-NP implants, while almost no dense bone tissue could be observed around Ti-SLA and Ti-OH implants (Fig. 7B). Meanwhile, quantitative analyses also showed the best outcomes regarding bone volume fraction (BV/TV), trabecular thickness (Tb.Th), trabecular number (Tb.N), trabecular separation/spacing (Tb.Sp), and bone mineral density (BMD) in the Ti-NP group (Fig. 7D–H). These results indicate a far more efficacious effect with Ti-NP on new bone formation under oxidative stress. H&E and Masson's Trichrome staining were further performed to evaluate the quality of newly formed bone tissue around the implants (Fig. 7C). H&E staining showed the thicker and denser bone matrix around Ti-NP implants. Likewise, more mature bone (red color) can be observed in the Ti-NP group compared to other groups, as evidenced by Masson's Trichrome staining. In addition, the parallel osteogenesis tendency can also be found in normal rats with Ti-SLA and Ti-NP implants (Fig. S10). Altogether, these *in vivo* results provide compelling evidence for the enhanced osteogenic performance of Ti-NP implants.

To assess the biosafety of the modified titanium implants, H&E staining of major organs (the heart, liver, spleen, lung, and kidney) was conducted after implantation for 28 days. No identifiable pathological changes were observed in all rats, affirming an excellent safety profile of Ti-NP implants *in vivo* (Fig. S11).

### 3.8. In vivo antioxidant and immunomodulatory evaluation

In view of such delightful outcomes regarding osseointegration using Ti-NP implants, we next sought to understand the underlying mechanisms. The above *in vitro* results have demonstrated that Ti-NP, with exceptional antioxidant and immunomodulatory capabilities, robustly prompts osteogenesis by reshaping the microenvironment. Therefore, we assessed the *in vivo* antioxidant and immunomodulatory effects of Ti-NP in the initial phase after implantation, when the immune response is most active. In the presence of diabetes, accumulated ROS contributes to oxidative damage, which may ultimately lead to biological complications of the implant [8]. Much lower levels of 4-HNE, an aldehydic lipid peroxidation product [68], were detected in the bone-implant interface of Ti-NP, implying its conspicuous ability to suppress oxidative stress (Fig. 8A and B). Analogous results were also found in the expression of 8-OHdG, an oxidative DNA damage marker (Fig. 8A and C) [69]. Taken together, the above data yield evidence that Ti-NP endowed with excellent redox capacity can reshape oxidative microenvironment, which is essential for bone remodeling.

The oxidative stress microenvironment is generally accompanied by the overactivation of dysfunctional M1 macrophages [59]. Accordingly, we ulteriorly explored whether Ti-NP implants could positively drive the functional reprogramming of macrophages *in vivo*. To this end, we immunohistochemically analyzed the expression of TNF-α and CD206. As depicted in Fig. 8D–F, compared with the other groups, the deposition of the pro-inflammatory signal TNF-α presented a remarkable decrease in the Ti-NP group, whereas it displayed a predominantly stronger distribution of CD206-positive macrophages. Different from inert interfaces, the C-Ca-SalB NPs functionalized implants exhibit more proactive immunomodulatory properties by effectively reversing the adverse pro-inflammatory condition and reprogramming the macrophages into the pro-regenerative M2 phenotype, thereby creating a favorable microenvironment for downstream cells, which is parallel with the conclusions of the *in vitro* experiments.

Taken together, the above data demonstrate that Ti-NP dominates the regulation of the immune microenvironment in the early phase after implantation, which significantly influences subsequent tissue repair and remodeling. During the initial implantation stage, the acidic milieu induced by diabetes and surgical procedures triggers rapid SalB release to combat ROS and correct pathological microenvironments. As the local microenvironment stabilizes, Ti-NP exhibits moderate immunomodulatory effects, thereby promoting osseointegration. Besides, the release of $Ca^{2+}$ could provide favorable conditions for osteogenesis. Our results reveal that Ti-NP achieves favorable osseointegration in both type 1 DM and healthy rats 4 weeks after implantation, indicating its efficacy and broad applicability. Although this surface treatment strategy may not be universally applicable to all complicated bone-related diseases, given the common feature of pH reduction in many pathological microenvironments (*e.g.*, osteoporosis, infections), the responsive drug delivery strategy of Ti-NP has broad potential applications across various physiological and pathological conditions. Further studies involving multiple animal models and clinical validation are warranted.

## 4. Conclusion

In the present study, we elaborately designed microenvironment-responsive nanoparticles (C-Ca-SalB NPs) functionalized titanium implants to improve their therapeutic performance under both physiological and oxidative pathological conditions. The unique coordination structure of C-Ca-SalB NPs imparts the modified implants with on-demand antioxidant and immunomodulatory effects. Under normal conditions, the functionalized implants display modest immunomodulatory effects with C-Ca-SalB NPs remaining stable. Importantly, with

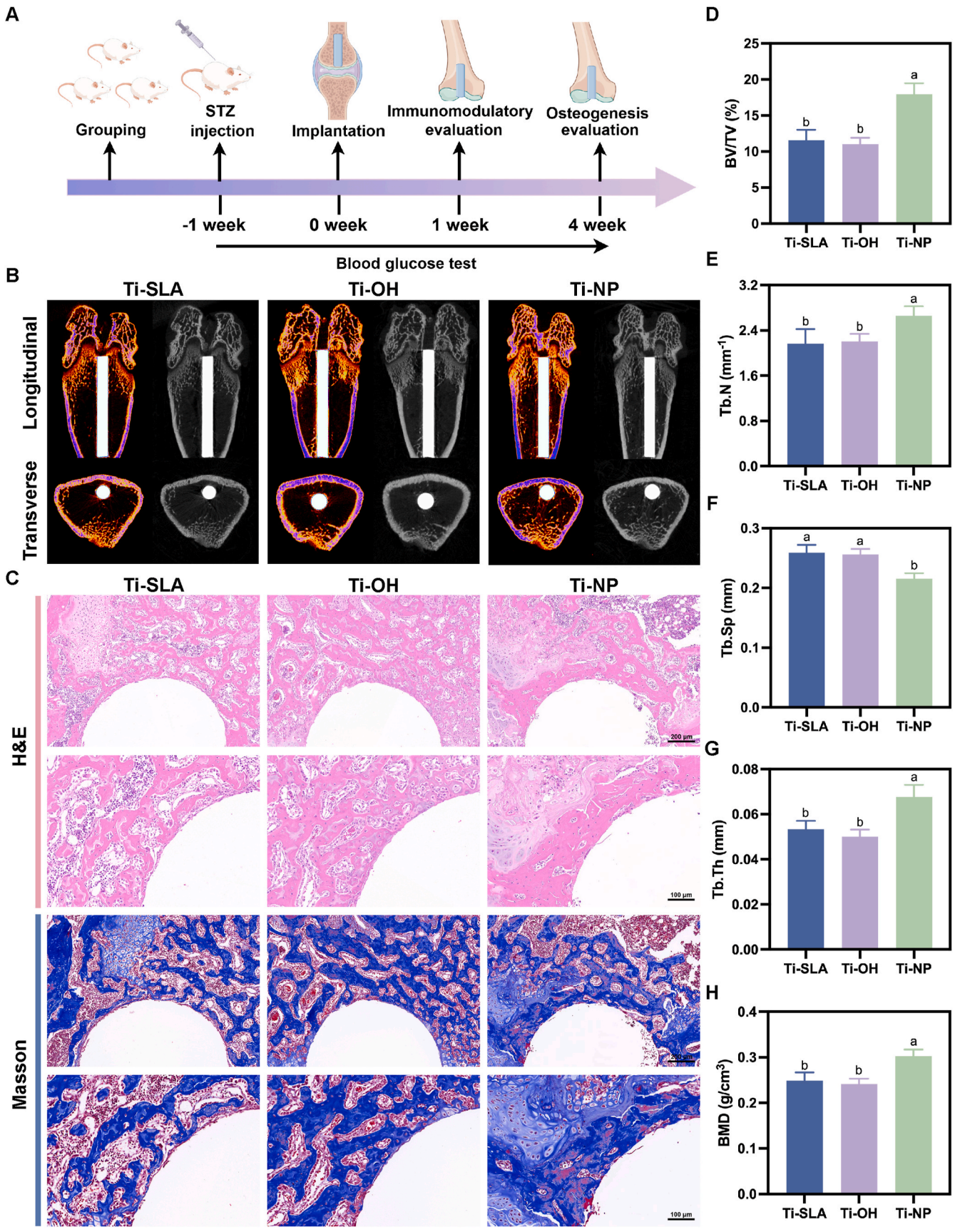


**Fig. 7.** Ti-NP promotes osseointegration in the DM-related oxidative stress rat model. (A). Schematic illustration of the establishment of the animal model and the *in vivo* study design. (B) Representative color-coded and gray-scale micro-CT images of femur samples after implantation for 4 weeks. (C) H&E and Masson's trichrome staining at the bone-implant interface after implantation for 4 weeks. Scale bars: 200 and 100 μm. (D–H) Quantitative analysis of BV/TV, Tb.N, Tb.Sp, Tb.Th, and BMD according to micro-CT data. Bars with different superscript letters indicate statistical differences ($P < 0.05$).

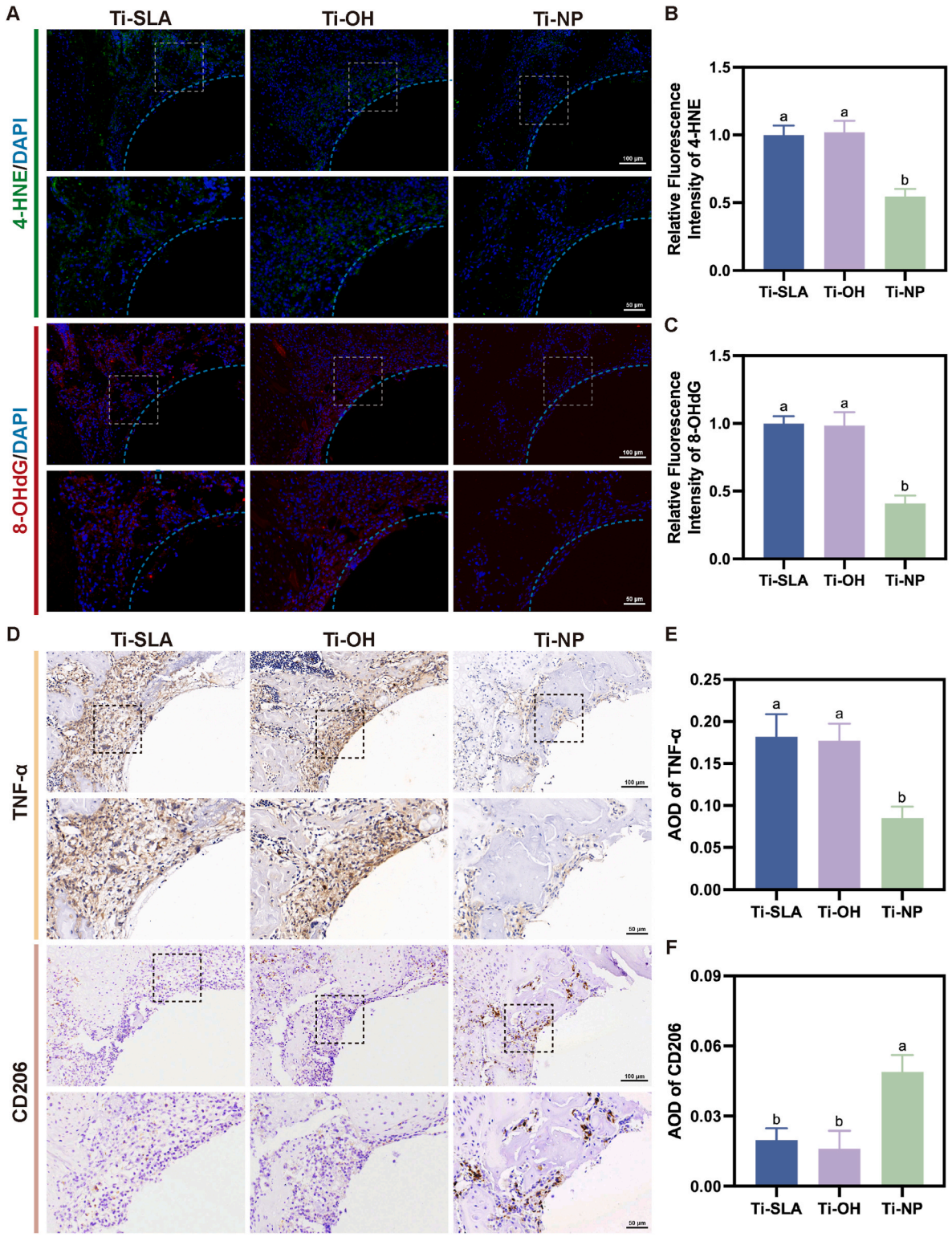


**Fig. 8.** *In vivo* antioxidant and immunoregulatory effects of Ti-NP. (A) Immunofluorescence staining of 4-HNE and 8-OHdG in the peri-implant tissue (blue dotted line: the bone-implant interface). Scale bars: 100 and 50 μm. (B, C) Relative fluorescence intensity of 4-HNE and 8-OHdG. (D) Representative immunohistochemical images of TNF-α and CD206 in the peri-implant tissue. Scale bars: 100 and 50 μm. (E, F) Quantitative analyses of the average optical density (AOD) for TNF-α and CD206 positive staining. Bars with different superscript letters indicate statistical differences ($P < 0.05$).

the stimulation of acidic oxidative conditions, C-Ca-SalB NPs loaded on the modified implants can disassemble rapidly, potently reversing the adverse oxidative microenvironment and creating a favorable condition by scavenging excess ROS and reprogramming macrophages from M1 to M2 phenotype. Overall, our results suggest that this novel modified implant provides an effective and broadly applicable strategy for improving implant therapy in various conditions, including challenging oxidative stress conditions, which might be widely utilized in future clinical applications.

## CRediT authorship contribution statement

**Wei Chen:** Writing – original draft, Methodology, Investigation, Formal analysis, Data curation, Conceptualization. **Yifei Pan:** Methodology, Investigation, Formal analysis, Data curation. **Catherine Huihan Chu:** Writing – review & editing, Formal analysis, Data curation. **Shuo Dong:** Investigation, Data curation. **Mingxi Wang:** Validation, Data curation. **Long Wang:** Validation, Data curation. **Lingxu Wang:** Visualization. **Xuyang Lin:** Software. **Chunbo Tang:** Writing – review & editing, Supervision, Resources, Project administration, Funding acquisition, Conceptualization.

## Declaration of competing interest

The authors declare that they have no known competing financial interests or personal relationships that could have appeared to influence the work reported in this paper.

## Acknowledgments

This work was supported by the National Natural Science Foundation of China (82170993). Fig.7A and Fig. S6A were created by Figdraw.

## Appendix A. Supplementary data

Supplementary data to this article can be found online at https://doi.org/10.1016/j.mtbio.2025.101628.

## Data availability

Data will be made available on request.

## References

[1] K. Gulati, D. Chopra, N.A. Kocak-Oztug, E. Verron, Fit and forget: the future of dental implant therapy via nanotechnology, Adv. Drug Delivery Rev. 199 (2023) 114900.
[2] J. Liu, B. Zhao, X. Shen, D. Lu, W. He, X. Zan, et al., Enhanced vascularization and osseointegration under osteoporotic conditions through functional peptide coating on implant surfaces, Mater. Today Bio 27 (2024) 101150.
[3] Q. He, S. Yuan, H. Tang, S. Wang, Z. Mu, D. Li, et al., Safeguarding osteointegration in diabetic patients: a potent "chain armor" coating for scavenging ROS and macrophage reprogramming in a microenvironment-responsive manner, Adv. Funct. Mater. 31 (31) (2021) 2101611.
[4] T. Aghaloo, J. Pi-Anfruns, A. Moshaverinia, D. Sim, T. Grogan, D. Hadaya, The effects of systemic diseases and medications on implant osseointegration: a systematic review, Int. J. Oral Maxillofac. Implants 34 (2019) s35–s49.
[5] J. Huang, R. Li, J. Yang, M. Cai, Y. Lee, A. Wang, et al., Bioadaptation of implants to in vitro and in vivo oxidative stress pathological conditions via nanotopography-induced FoxO1 signaling pathways to enhance osteoimmunal regeneration, Bioact. Mater. 6 (10) (2021) 3164–3176.
[6] G. Guabello, F. Zuffetti, A. Ravidà, M. Deflorian, G. Carta, M.H.A. Saleh, et al., Avoiding implant-related complications in medically compromised patients with or without unhealthy lifestyle/elevated oxidative stress, Periodontol 92 (1) (2000 2023) 329–349.
[7] P. de Oliveira, E.A. Bonfante, E.T.P. Bergamo, S.L.S. de Souza, L. Riella, A. Torroni, et al., Obesity/metabolic syndrome and diabetes mellitus on peri-implantitis, Trends Endocrinol. Metab. 31 (8) (2020) 596–610.
[8] N. Sheng, F. Xing, J. Wang, Q.Y. Zhang, R. Nie, J. Li-Ling, et al., Recent progress in bone-repair strategies in diabetic conditions, Mater. Today Bio 23 (2023) 100835.
[9] W. Jiang, X. Hou, Y. Qi, Z. Wang, Y. Liu, X.J. Gao, et al., pH-activatable pre-nanozyme mediated $H_2S$ delivery for endo-exogenous regulation of oxidative stress in acute kidney injury kidney injury, Adv. Sci. 11 (18) (2024) e2303901.
[10] R. Yang, Y. Yan, Z. Wu, Y. Wei, H. Song, L. Zhu, et al., Resveratrol-loaded titania nanotube coatings promote osteogenesis and inhibit inflammation through reducing the reactive oxygen species production via regulation of NF-κB signaling pathway, Mater. Sci. Eng. C, Mater. Biol. Appl. 131 (2021) 112513.
[11] Y. Chen, W. Gan, Z. Cheng, A. Zhang, P. Shi, Y. Zhang, Plant molecules reinforce bone repair: novel insights into phenol-modified bone tissue engineering scaffolds for the treatment of bone defects, Mater. Today Bio 24 (2024) 100920.
[12] M. Tsukasaki, H. Takayanagi, Osteoimmunology: evolving concepts in bone-immune interactions in health and disease, Nat. Rev. Immunol. 19 (10) (2019) 626–642.
[13] L. Tong, AJv Wijnen, H. Wang, D. Chen, Advancing bone biology: the mutual promotion of biology and pioneering technologies, The Innovation Life 2 (3) (2024) 100078.
[14] Y. Wang, Z. Li, R. Yu, Y. Chen, D. Wang, W. Zhao, et al., Metal-phenolic network biointerface-mediated cell regulation for bone tissue regeneration, Mater. Today Bio 30 (2025) 101400.
[15] H. Wang, Y. Zhang, Y. Zhang, C. Li, M. Zhang, J. Wang, et al., Activating macrophage continual efferocytosis via microenvironment biomimetic short fibers for reversing inflammation in bone repair, Adv. Mater. 36 (30) (2024) 2402968.
[16] Q. Zhang, W. Chen, G. Li, Z. Ma, M. Zhu, Q. Gao, et al., A factor-free hydrogel with ros scavenging and responsive degradation for enhanced diabetic bone healing, Small 20 (24) (2024) 2306389.
[17] Q. Zhang, M. Xin, S. Yang, Q. Wu, X. Xiang, T. Wang, et al., Silica nanocarrier-mediated intracellular delivery of rapamycin promotes autophagy-mediated M2 macrophage polarization to regulate bone regeneration, Mater. Today Bio 20 (2023) 100623.
[18] Y. Chen, W. Zhao, A. Hu, S. Lin, P. Chen, B. Yang, et al., Type 2 diabetic mellitus related osteoporosis: focusing on ferroptosis, J. Transl. Med. 22 (1) (2024) 409.
[19] Q. Lihao, L. Tingting, Z. Jiawei, B. Yifei, T. Zheyu, L. Jingyan, et al., 3D bioprinting of salvianolic acid B-sodium alginate-gelatin skin scaffolds promotes diabetic wound repair via antioxidant, anti-inflammatory, and proangiogenic effects, Biomed. Pharmacother. 171 (2024) 116168.
[20] G. He, G. Chen, W. Liu, D. Ye, X. Liu, X. Liang, et al., Salvianolic acid B: a review of pharmacological effects, safety, combination therapy, new dosage forms, and novel drug delivery routes, Pharmaceutics 15 (9) (2023) 2235.
[21] K.Y. Wong, Z. Nie, M.S. Wong, Y. Wang, J. Liu, Metal-drug coordination nanoparticles and hydrogels for enhanced delivery, Adv. Mater. 36 (26) (2024) e2404053.
[22] M. Chen, D. Wang, M. Li, Y. He, T. He, M. Chen, et al., Nanocatalytic biofunctional mof coating on titanium implants promotes osteoporotic bone regeneration through cooperative pro-osteoblastogenesis msc reprogramming, ACS Nano 16 (9) (2022) 15397–15412.
[23] Y. Guo, Q. Sun, F.-G. Wu, Y. Dai, X. Chen, Polyphenol-containing nanoparticles: synthesis, properties, and therapeutic delivery, Adv. Mater. 33 (22) (2021) 2007356.
[24] K. Kim, J.H. Ryu, D.Y. Lee, H. Lee, Bio-inspired catechol conjugation converts water-insoluble chitosan into a highly water-soluble, adhesive chitosan derivative for hydrogels and LB assembly, Biomater. Sci. 1 (7) (2013) 783–790.
[25] W. Chen, X. Shen, Y. Hu, K. Xu, Q. Ran, Y. Yu, et al., Surface functionalization of titanium implants with chitosan-catechol conjugate for suppression of ros-induced cells damage and improvement of osteogenesis, Biomaterials 114 (2017) 82–96.
[26] L.J. Huang, S.H. Lin, T.Y. Chen, S.H. Hsu, Chitosan catechol-tannic acid composite hydrogel and cryogel with antimicrobial and hemostatic properties, Int. J. Biol. Macromol. 270 (Pt 2) (2024) 132174.
[27] F. Novio, J. Simmchen, N. Vázquez-Mera, L. Amorín-Ferré, D. Ruiz-Molina, Coordination polymer nanoparticles in medicine, Coord. Chem. Rev. 257 (19) (2013) 2839–2847.
[28] B. Chen, W. Wang, M. Hu, Y. Liang, N. Wang, C. Li, et al., "Photo-thermo-electric" dental implant for anti-infection and enhanced osteoimmunomodulation, ACS Nano 18 (36) (2024) 24968–24983.
[29] Y. Shan, F. Cao, X. Zhao, J. Luo, H. Mei, L. Zhang, et al., Procoagulant, antibacterial and antioxidant high-strength porous hydrogel adhesives in situ formed via self-gelling hemostatic microsheets for emergency hemostasis and wound repair, Biomaterials 315 (2024) 122936.
[30] J.H. Ryu, S. Hong, H. Lee, Bio-inspired adhesive catechol-conjugated chitosan for biomedical applications: a mini review, Acta Biomater. 27 (2015) 101–115.
[31] H. He, C. Sun, Y. Weng, H. Huang, P. Ni, Y. Fang, et al., Catechol modification of non-woven chitosan gauze for enhanced hemostatic efficacy, Carbohydr. Polym. 286 (2022) 119319.
[32] W. Cao, J. Yan, C. Liu, J. Zhang, H. Wang, X. Gao, et al., Preparation and characterization of catechol-grafted chitosan/gelatin/modified chitosan-AgNP blend films, Carbohydr. Polym. 247 (2020) 116643.
[33] B. Lu, D. Luo, A. Zhao, H. Wang, Y. Zhao, M.F. Maitz, et al., pH responsive chitosan and hyaluronic acid layer by layer film for drug delivery applications, Prog. Org. Coat. 135 (2019) 240–247.
[34] X. Wang, L. Lv, T. Liu, F. Yang, X. Han, Q. Guan, Catechol chitosan coated dual-loaded liposomes based on oxidation and saccharification mechanisms for enhancing skin anti-aging effects, Int. J. Biol. Macromol. 256 (Pt 2) (2024) 128342.
[35] K. Wang, K. Jiang, C. Luo, X. You, H.-Y. Shen, D. Wu, et al., An osteoimmunomodulatory $Ca^{2+}/Zn^{2+}$-doped scaffold promotes M2 macrophage polarization via the src-mediated chemoking signaling pathway to enhance osteoinduction, Compos. B Eng. 284 (2024) 111653.
[36] Z. Yang, N.J. Leon, C. Liao, B.J. Ingram, L. Trahey, Effect of salt concentration on the interfacial solvation structure and early stage of solid-electrolyte interphase formation in $Ca(BH_4)_2$/THF for Ca batteries, ACS Appl. Mater. Interfaces 15 (20) (2023) 25018–25028.
[37] M. Wen, T. Wang, N. Li, Y. Wu, L. Zhang, Y. Xue, et al., Polyphenol-copper derived self-cascade nanozyme hydrogel in boosting oxygenation and robust revascularization for tissue regeneration, Adv. Funct. Mater. 34 (2024) 2403634.
[38] J. Bian, T. Wu, Q. Zhou, H. Xie, C. Chen, Silane-coupled chitosan-cyclodextrin/rosmarinic acid-zinc complex coating improves the osseointegration of titanium implants in high-glucose environments, Appl. Surf. Sci. 638 (2023) 158015.
[39] W. Pi, L. Wu, J. Lu, X. Lin, X. Huang, Z. Wang, et al., A metal ions-mediated natural small molecules carrier-free injectable hydrogel achieving laser-mediated photo-fenton-like anticancer therapy by synergy apoptosis/cuproptosis/anti-inflammation, Bioact. Mater. 29 (2023) 98–115.
[40] M. He, X. Zhang, X. Ran, Y. Zhang, X. Nie, B. Xiao, et al., Black phosphorus nanosheets protect neurons by degrading aggregative α-syn and clearing ROS in Parkinson's disease, Adv. Mater. 36 (30) (2024) 2404576.

[41] J. Yang, C. Liu, H. Sun, Y. Liu, Z. Liu, D. Zhang, et al., The progress in titanium alloys used as biomedical implants: from the view of reactive oxygen species, Front. Bioeng. Biotechnol. 10 (2022) 1092916.
[42] Q. Chen, J. Li, F. Han, Q. Meng, H. Wang, Q. Wei, et al., A multifunctional composite hydrogel that rescues the ROS microenvironment and guides the immune response for repair of osteoporotic bone defects, Adv. Funct. Mater. 32 (27) (2022) 2201067.
[43] V. Rani, G. Deep, R.K. Singh, K. Palle, U.C. Yadav, Oxidative stress and metabolic disorders: pathogenesis and therapeutic strategies, Life Sci. 148 (2016) 183–193.
[44] R.S.B. Lee, S.M. Hamlet, H.J. Moon, S. Ivanovski, Re-establishment of macrophage homeostasis by titanium surface modification in type II diabetes promotes osseous healing, Biomaterials 267 (2021) 120464.
[45] F. Rupp, L. Liang, J. Geis-Gerstorfer, L. Scheideler, F. Hüttig, Surface characteristics of dental implants: a review, Dent. Mater. 34 (1) (2018) 40–57.
[46] J. Dong, F. Chen, Y. Yao, C. Wu, S. Ye, Z. Ma, et al., Bioactive mesoporous silica nanoparticle-functionalized titanium implants with controllable antimicrobial peptide release potentiate the regulation of inflammation and osseointegration, Biomaterials 305 (2024) 122465.
[47] Y. Chen, X. Ning, X. Jia, H. Xin, S. Kong, B. Wu, et al., Hydrophobic coating platforms for high-efficiency loading and direct transmembrane delivery of fat-soluble osteogenic drug for enhanced osseointegration of titanium implants, Adv. Funct. Mater. 34 (18) (2024) 2314005.
[48] Z. Yang, Y. Xi, J. Bai, Z. Jiang, S. Wang, H. Zhang, et al., Covalent grafting of hyperbranched poly-L-lysine on Ti-based implants achieves dual functions of antibacteria and promoted osteointegration in vivo, Biomaterials 269 (2021) 120534.
[49] J. Chen, G. Hu, T. Li, Y. Chen, M. Gao, Q. Li, et al., Fusion peptide engineered "statically-versatile" titanium implant simultaneously enhancing anti-infection, vascularization and osseointegration, Biomaterials 264 (2021) 120446.
[50] Z. Du, F. Qiao, L. Tong, W. Zhang, X. Mou, X. Zhao, et al., Mimicking mytilus edulis foot protein: a versatile strategy for robust biomedical coatings, Innovation 5 (5) (2024) 100671.
[51] J. da Rocha, E.D. de Avila, M.S.M. Rigolin, P.A. Barbugli, D.O.M. Marin, F.A. Mollo Junior, et al., Biological and physicochemical implications of the aging process on titanium and zirconia implant material surfaces, J. Prosthet. Dent 125 (1) (2021) 165–174.
[52] D. Kido, K. Komatsu, T. Suzumura, T. Matsuura, J. Cheng, J. Kim, et al., Influence of surface contaminants and hydrocarbon pellicle on the results of wettability measurements of titanium, Int. J. Mol. Sci. 24 (19) (2023) 14688.
[53] Y. Xu, Z. Shen, Y. Zhou, Y.H. Zhou, J.Y. Zhou, X.N. Qian, et al., Osteogenic and anti-inflammatory effects of sla titanium substrates doped with chitosan-stabilized selenium nanoparticles via a covalent coupling strategy, Colloids Surf., B 224 (2023) 113217.
[54] Q. Zhou, T. Wu, Z. Bai, G. Hong, J. Bian, H. Xie, et al., A silane-based coupling strategy for enhancing the mechanical properties of proanthocyanidin nanocoatings on ti dental implants, Appl. Surf. Sci. 602 (2022) 154400.
[55] R.J. Miron, M. Bohner, Y. Zhang, D.D. Bosshardt, Osteoinduction and osteoimmunology: emerging concepts, Periodontol 94 (1) (2000 2024) 9–26.
[56] J. Yang, H. Zhang, S.M. Chan, R. Li, Y. Wu, M. Cai, et al., $TiO_2$ nanotubes alleviate diabetes-induced osteogenetic inhibition, Int. J. Nanomed. 15 (2020) 3523–3537.
[57] X. Shen, K. Fang, K.H. Ru Yie, Z. Zhou, Y. Shen, S. Wu, et al., High proportion strontium-doped micro-arc oxidation coatings enhance early osseointegration of titanium in osteoporosis by anti-oxidative stress pathway, Bioact. Mater. 10 (2022) 405–419.
[58] J. Li, X. Jiang, H. Li, M. Gelinsky, Z. Gu, Tailoring materials for modulation of macrophage fate, Adv. Mater. 33 (12) (2021) 2004172.
[59] C. Xue, J. Tian, Z. Cui, Y. Liu, D. Sun, M. Xiong, et al., Reactive oxygen species (ROS)-mediated m1 macrophage-dependent nanomedicine remodels inflammatory microenvironment for osteoarthritis recession, Bioact. Mater. 33 (2024) 545–561.
[60] Y. Xiong, B.B. Mi, Z. Lin, Y.Q. Hu, L. Yu, K.K. Zha, et al., The role of the immune microenvironment in bone, cartilage, and soft tissue regeneration: from mechanism to therapeutic opportunity, Mil. Med. Res. 9 (1) (2022) 65.
[61] J.O. Abaricia, A.H. Shah, M. Chaubal, K.M. Hotchkiss, R. Olivares-Navarrete, Wnt signaling modulates macrophage polarization and is regulated by biomaterial surface properties, Biomaterials 243 (2020) 119920.
[62] L. Xie, G. Wang, Y. Wu, Q. Liao, S. Mo, X. Ren, et al., Programmed surface on poly (aryl-ether-ether-ketone) initiating immune mediation and fulfilling bone regeneration sequentially, Innovation 2 (3) (2021) 100148.
[63] C. Ji, L. Bi, J. Li, J. Fan, Salvianolic acid B-loaded chitosan/hydroxyapatite scaffolds promotes the repair of segmental bone defect by angiogenesis and osteogenesis, Int. J. Nanomed. 14 (2019) 8271–8284.
[64] W. Wang, Y. Liu, C. Yang, W. Jia, X. Qi, C. Liu, et al., Delivery of salvianolic acid B for efficient osteogenesis and angiogenesis from silk fibroin combined with graphene oxide, ACS Biomater. Sci. Eng. 6 (6) (2020) 3539–3549.
[65] C. Liu, W. Liu, B. Qi, L. Fan, S. Liu, Q. Yang, et al., Bone homeostasis modulating orthopedic adhesive for the closed-loop management of osteoporotic fractures, Small 19 (48) (2023) e2302704.
[66] F. Qi, H. Huang, M. Wang, W. Rong, J. Wang, Applications of antioxidants in dental procedures, Antioxidants 11 (12) (2022) 2492.
[67] P. Żukowski, M. Maciejczyk, D. Waszkiel, Sources of free radicals and oxidative stress in the oral cavity, Arch. Oral Biol. 92 (2018) 8–17.
[68] M. Jaganjac, L. Milkovic, N. Zarkovic, K. Zarkovic, Oxidative stress and regeneration, Free Radical Biol. Med. 181 (2022) 154–165.
[69] Z. Yuan, J. Wu, Z. Fu, S. Meng, L. Dai, K. Cai, Polydopamine-mediated interfacial functionalization of implants for accelerating infected bone repair through light-activatable antibiosis and carbon monoxide gas regulated macrophage polarization, Adv. Funct. Mater. 32 (27) (2022) 2200374.